UC San Diego
UC San Diego Previously Published Works

Title

Unveiling the Role of the Most Impactful Cardiovascular Risk Locus through Haplotype Editing

Permalink

Journal

ISSN

Authors

Lo Sardo, Valentina
Chubukov, Pavel
Ferguson, William
et al.

Publication Date

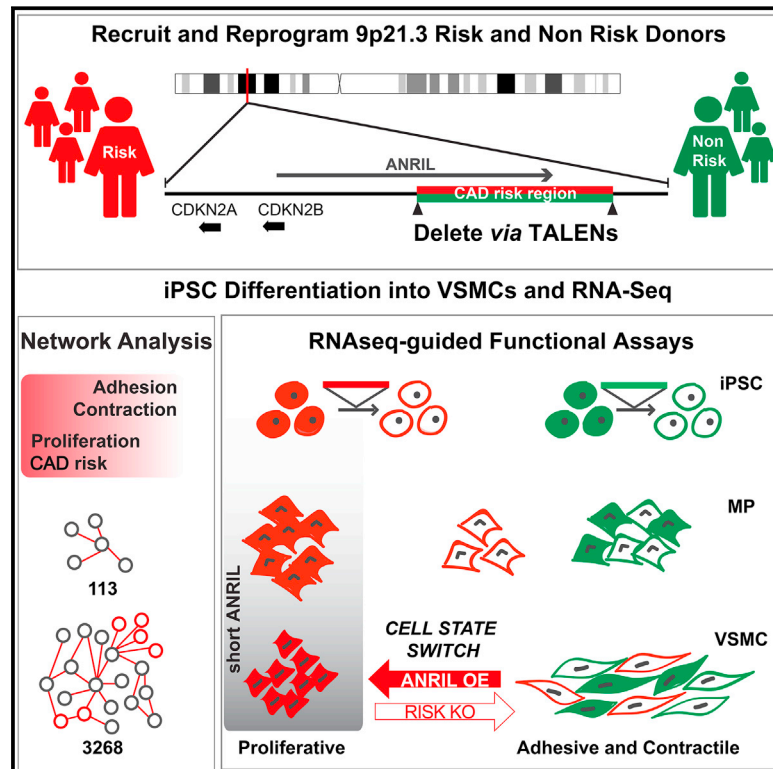**DOI**

Peer reviewed

Unveiling the Role of the Most Impactful Cardiovascular Risk Locus through Haplotype Editing

Graphical Abstract

Highlights

- Profiling iPSC-derived VSMCs uncovers CAD risk haplotype-dependent phenotypes

- Deleting the risk haplotype rescues VSMC proliferation, adhesion, and contraction

- Risk-dependent gene networks drive cell state instability, partially through *ANRIL*

- Evidence for cross-talk between CAD risk loci predicts vascular therapeutic targets

Authors

Valentina Lo Sardo, Pavel Chubukov, William Ferguson, ..., Eric J. Topol, Ali Torkamani, Kristin K. Baldwin

Correspondence

kbaldwin@scripps.edu

In Brief

Genome editing and iPSC-based modeling of the 9p21.3 cardiovascular disease locus shows that it controls large gene networks acting in vascular smooth muscle cells that predispose them to assume atherogenic-like cell states.

Unveiling the Role of the Most Impactful Cardiovascular Risk Locus through Haplotype Editing

Valentina Lo Sardo,[1,8] Pavel Chubukov,[1,8,11] William Ferguson,[1] Aditya Kumar,[6] Evan L. Teng,[6] Michael Duran,[1] Lei Zhang,[5] Gregory Cost,[5,10] Adam J. Engler,[6,7] Fyodor Urnov,[5,9] Eric J. Topol,[2,4] Ali Torkamani,[2,3] and Kristin K. Baldwin[1,12,*]

[1]Department of Neuroscience, The Scripps Research Institute, La Jolla, CA 92037, USA
[2]Scripps Research Translational Institute, The Scripps Research Institute, La Jolla, CA, 92037, USA
[3]Department of Integrative Structural and Computational Biology, The Scripps Research Institute, La Jolla, CA 92037, USA
[4]Department of Molecular Medicine, The Scripps Research Institute, La Jolla, CA 92037, CA
[5]Sangamo BioSciences, Inc., Richmond, CA 94804-3517, USA
[6]Department of Bioengineering, University of California San Diego, La Jolla, CA 92093-0412, USA
[7]Sanford Consortium for Regenerative Medicine, La Jolla, CA 92037, USA
[8]These authors contributed equally
[9]Present address: Altius Institute for Biomedical Sciences, Seattle, WA 98121, USA
[10]Present address: Casebia Therapeutics, San Francisco, CA 94158, USA
[11]Present address: MuWells, Inc., San Diego, CA 92121, USA
[12]Lead Contact
*Correspondence: kbaldwin@scripps.edu
https://doi.org/10.1016/j.cell.2018.11.014

SUMMARY

The 9p21.3 cardiovascular disease locus is the most influential common genetic risk factor for coronary artery disease (CAD), accounting for ~10%–15% of disease in non-African populations. The ~60 kb risk haplotype is human-specific and lacks coding genes, hindering efforts to decipher its function. Here, we produce induced pluripotent stem cells (iPSCs) from risk and non-risk individuals, delete each haplotype using genome editing, and generate vascular smooth muscle cells (VSMCs). Risk VSMCs exhibit globally altered transcriptional networks that intersect with previously identified CAD risk genes and pathways, concomitant with aberrant adhesion, contraction, and proliferation. Unexpectedly, deleting the risk haplotype rescues VSMC stability, while expressing the 9p21.3-associated long non-coding RNA *ANRIL* induces risk phenotypes in non-risk VSMCs. This study shows that the risk haplotype selectively predisposes VSMCs to adopt a cell state associated with CAD phenotypes, defines new VSMC-based networks of CAD risk genes, and establishes haplotype-edited iPSCs as powerful tools for functionally annotating the human genome.

INTRODUCTION

Cardiovascular disease (CVD), in particular coronary artery disease (CAD), remains the largest worldwide cause of death. While current therapies focus on addressing the role of cholesterol and lifestyle in CVD, recent human genetic studies have identified a set of ~100 genetic variants that influence CAD risk (Nikpay et al., 2015). Intriguingly, based on tissue expression profiles, many of these variants appear to act in the vascular wall, although no clear mechanisms for this have been defined (Howson et al., 2017). The first discovered and most impactful CVD risk locus spans an ~60 kb 9p21.3 chromosomal region linked to several CVDs, including CAD, stroke, and aneurysms (Burton et al., 2007; Helgadottir et al., 2007; McPherson and Tybjaerg-Hansen, 2016; McPherson et al., 2007; Nikpay et al., 2015; Samani et al., 2007). In contrast to disease risk mediated by a single causal DNA variant, the 9p21.3 locus comprises two ~60 kb haplotypes (risk versus non-risk), which are blocks of ~50–100 single-nucleotide polymorphisms (SNPs) in linkage disequilibrium, that segregate together in most non-African populations. In many populations, the frequency of the risk haplotype is ~50%. The prevalence and strong additive effect of each copy of the risk haplotype results in an estimated population fraction of 10%–15% of CAD incidence in the United States, thereby representing the largest known genomic source of healthcare costs and lost labor in the United States (Gränsbo et al., 2013).

9p21.3-based genetic risk appears independent of cholesterol levels or other known clinical risk factors and is not directly linked to myocardial infarction (Gschwendtner et al., 2009). Rather, association studies suggest that this risk haplotype acts to promote early events leading to atherosclerotic plaque formation (Bennett et al., 2016; Miller et al., 2016; Motterle et al., 2012). Vascular smooth muscle cells (VSMCs) are a strongly implicated cell type in this process. During early stages of CAD, mature contractile VSMCs that play key roles in maintaining vascular tone can also de-differentiate into a variety of cell states (sometimes termed synthetic VSMCs) that are more proliferative, less

contractile and adhesive, and play key roles in plaque formation and stability (Alexander and Owens, 2012; Bennett et al., 2016). Indeed, recent mouse lineage tracing studies found that VSMC-derived cells can comprise ~80% of cells found in plaques, possibly even including foam cells, previously thought to derive solely from the macrophage lineage (Bennett et al., 2016; Shankman et al., 2015). The 9p21.3 risk haplotype has also been linked to atherosclerotic stroke, as well as other CVDs thought to involve VSMC functions, such as abdominal aortic and intracranial aneurysms (Helgadottir et al., 2008; Dichgans et al., 2014).

Despite its unique impact on human health, the function of the 9p21.3 risk locus in CAD remains enigmatic. Several factors have hindered efforts to decipher the functional consequences of this region. First, the 9p21.3 CVD genomic region is poorly syntenic in rodents, with clear human synteny emerging only in primates (He et al., 2013; Jarinova et al., 2009; Visel et al., 2010). Second, this region is a gene desert, lacking known coding genes, with the closest genes being the cell-cycle inhibitors *CDKN2A* and *CDKN2B*. Third, although the region encompasses the terminal exons of a long non-coding RNA (lncRNA), *ANRIL* (also known as *CDKN2B-AS1*), and is predicted to be enhancer rich, both lncRNA function and enhancer activity are difficult to assess using purely computational tools and are often highly context-dependent (Hannou et al., 2015; Chen et al., 2014).

To investigate this locus, one group performed a complete deletion of the *Cdkn2a/b* adjacent region in mice, which is the closest region to the human risk haplotype. These mice exhibited increased tumor incidence, early death, and increased cell proliferation but not atherosclerosis (Visel et al., 2010). Human correlative studies of 9p21.3 function in various cell types have reported variable and conflicting results. For example, a study of peripheral blood from 1,134 patients with CAD showed that the risk region correlated with increased *ANRIL* but had no effect on *CDKN2A* or *CDKN2B* (Holdt et al., 2010), while a study of peripheral T cells in 170 healthy donors linked the risk haplotype to reduced *ANRIL* and *CDKN2A/B* (Liu et al., 2017). An additional confounding factor is that *ANRIL* is extensively alternatively spliced. Because differences in splice isoforms can depend on the cell type and state, this leads to difficulties in directly comparing studies using different *ANRIL* primer sets in different cell lineages (Hannou et al., 2015; Holdt and Teupser, 2012; Holdt et al., 2011, 2013; Jarinova et al., 2009; Motterle et al., 2012). Given this heterogeneity, performing studies in a strongly implicated cell type such as human VSMCs would likely be most informative. However, such studies have been limited by difficulties in obtaining patient coronary arteries, by the tendency of VSMCs to senesce *in vitro* and by the known phenotypic heterogeneity of VSMCs across individuals, tissues, and disease states (Almontashiri et al., 2015).

To overcome these obstacles, we applied genome editing to fully delete the genetically defined CAD risk and non-risk haplotypes (haplotype editing) in iPSCs (induced pluripotent stem cells) and generated a large cohort of 19 isogenic lines. Notably, we achieved efficient homozygous deletion of the entire ~60 kb haplotype in iPSCs from risk and non-risk individuals. To precisely define the cellular impact of the locus in disease-relevant cells, while reducing sources of experimental noise, we differentiated iPSCs into VSMCs under identical culture conditions and performed RNA sequencing (RNA-seq) throughout differentiation. These studies identified a network of ~3,000 genes that are driven by presence of the risk haplotype and that are implicated in cell proliferation, adhesion, and contraction. Surprisingly, while deleting the risk haplotype nearly completely restored VSMCs to the non-risk state, deletion of the non-risk region had minimal effect, suggesting that the risk haplotype exerts an additive gain of function effect based on only a small number (59–100) of single nucleotide changes across a 60 kb region.

Guided by the transcriptomic results, we functionally tested the VSMCs and showed that risk-dependent VSMCs are phenotypically distinct from non-risk cells and display reduced contraction and adhesion as well as increased proliferation, recapitulating key phenotypes of the de-differentiated synthetic VSMCs found in atherosclerotic plaques. We also identified candidate pathogenic isoforms of *ANRIL* expressed in risk VSMCs, which, when overexpressed in non-risk VSMCs, induce a synthetic-like cell state. Based on these results, we propose a model in which the 9p21.3 risk haplotype acts additively to increase the propensity for VSMCs to de-differentiate and/or to directly impair mature VSMC functions including adhesion, contraction, and proliferation, thereby influencing risk for CAD and possibly other CVDs. Finally, we show that in VSMCs, the risk locus influences expression of 38 of the 91 known CAD risk genes identified in GWAS studies (Nikpay et al., 2015; Howson et al., 2017). These studies define a new VSMC-based gene network linking the risk haplotype to a cell state shift in VSMCs involving more than a third of known CAD risk genes, potentially opening the door to new arterial wall-focused therapeutic interventions. Accordingly, this study validates the power of haplotype editing in human iPSCs to uncover new functions of human-specific and non-coding genomic regions relevant to human-specific genome biology and disease.

RESULTS

Efficient Deletion of the ~60 kb 9p21.3 Haplotype in iPSCs

To establish the impact of the different 9p21.3 CVD risk haplotypes (Figure 1A), we generated iPSCs from CVD patients who were homozygous for the risk haplotype (RR) and from healthy individuals who were homozygous for the non-risk haplotype (NN) (Figure 1B; STAR Methods) (Lo Sardo et al., 2017). The CVD risk locus comprises an ~60 kb block of SNPs in linkage disequilibrium (Figure 1A; Table S1), thus it is unclear which SNPs influence disease risk (Shea et al., 2011). Therefore, our goal was to delete the entire haplotype (referred to as haplotype editing) (Carroll, 2014). Precise genome deletions can be generated using zinc finger nucleases, TALENs, or CRISPR/Cas9 type nucleases to induce double strand breaks at two sites of the same chromatid (Lee et al., 2010; Liu et al., 2010). However, the likelihood of success, maximum size, and reproducibility of large-scale genomic deletions remain poorly defined.

Here, we engineered and tested multiple sets of TALENs and, to provide a control for off-target effects, selected the two
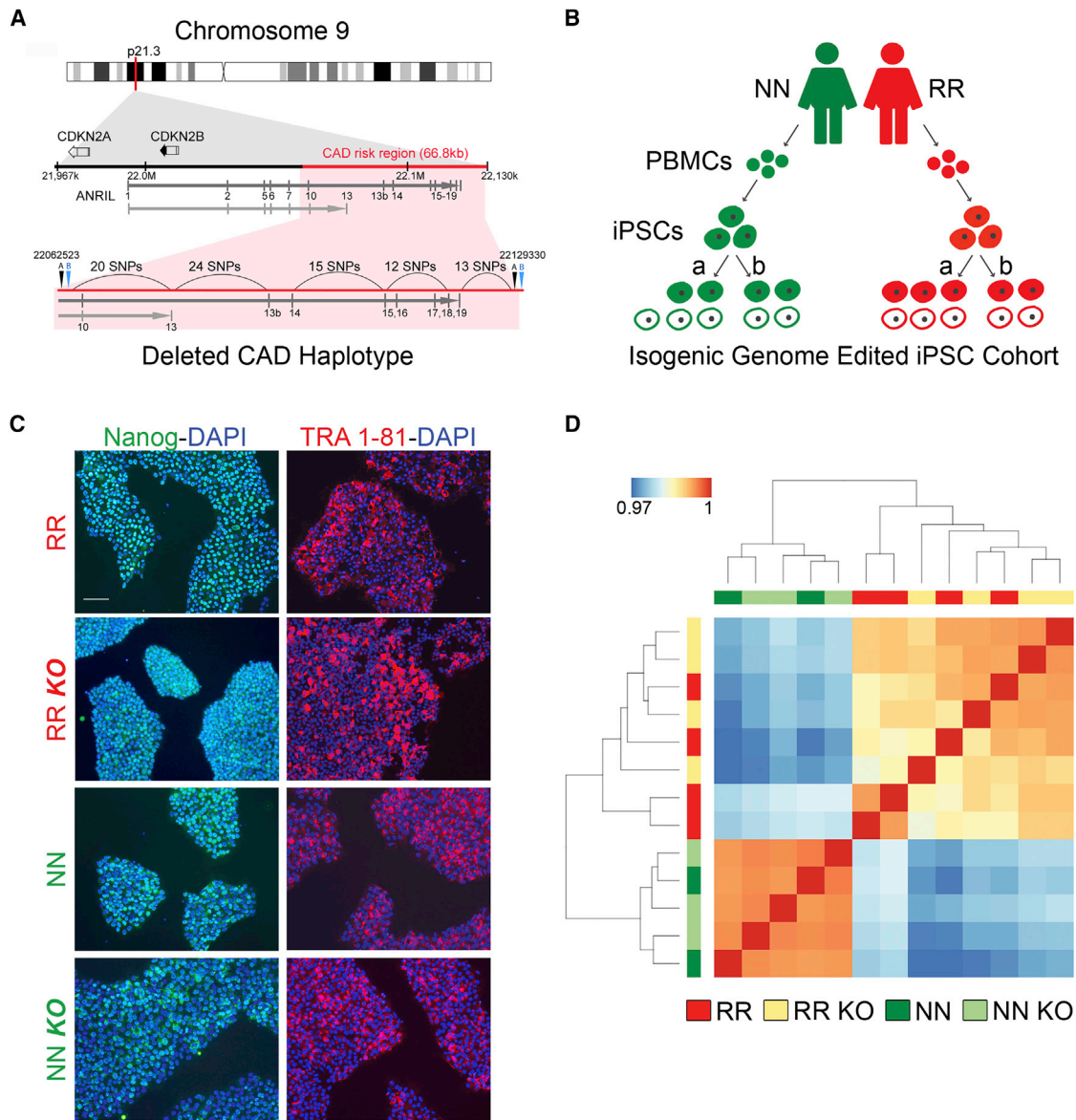
Figure 1. Genome Editing of 9p21 CVD Region in hiPSCs

(A) Schematic of the 9p21.3 CVD risk region, and the approximate cut sites for the two pairs of TALENS (black and blue triangles). The arches denote regions containing the number of SNPs indicated above.

(B) Experimental design overview for the generation of isogenic cohorts of 9p21-deleted iPSC lines. Peripheral blood was collected from individuals homozygous risk (RR-red) or non–risk (NN-green) for 9p21.3 CAD-risk region. PBMCs were expanded and reprogrammed into iPSCs. Two independent TALENS sets (a or b) were used to generate isogenic knock out (KO) iPSC lines (open circles) or unedited control clones (filled circles). Nine NN-derived 10 RR-derived total lines were selected for further analysis.

(C) Immunocytochemistry for Nanog (green), TRA1-81 (red), and DAPI (blue) in isogenic lines from RR and RR KO, NN, and NN KO. Scale bar, 100 μm.

(D) Heatmap of RNA-seq data showing hierarchical clustering of iPSCs based on patient genotype.

See also Figure S1 and Tables S1 and S2.

independent pairs for iPSC-based editing (Figures 1A and 1B; Table S1; STAR Methods). Both sets of TALENs readily produced the expected ∼60 k homozygous and heterozygous 9p21.3 deletions, without selectable markers (Figures S1A–S1C and S1E). Homozygous deletion of this locus did not significantly impact iPSC growth rates or pluripotency marker expression (Figure 1C). No genes were significantly differentially expressed in isogenic control versus knockout pairs (Figure 1D). To sensitively detect phenotypes that could be masked by inter-human genetic variation or by epigenetic variation among iPSCs, we established a large "test" set of 19 wild-type (WT) and knockout (KO) isogenic iPSC lines derived from one risk and one non-risk individual using lines edited with both TALEN sets (Figure 1B; Table S2).
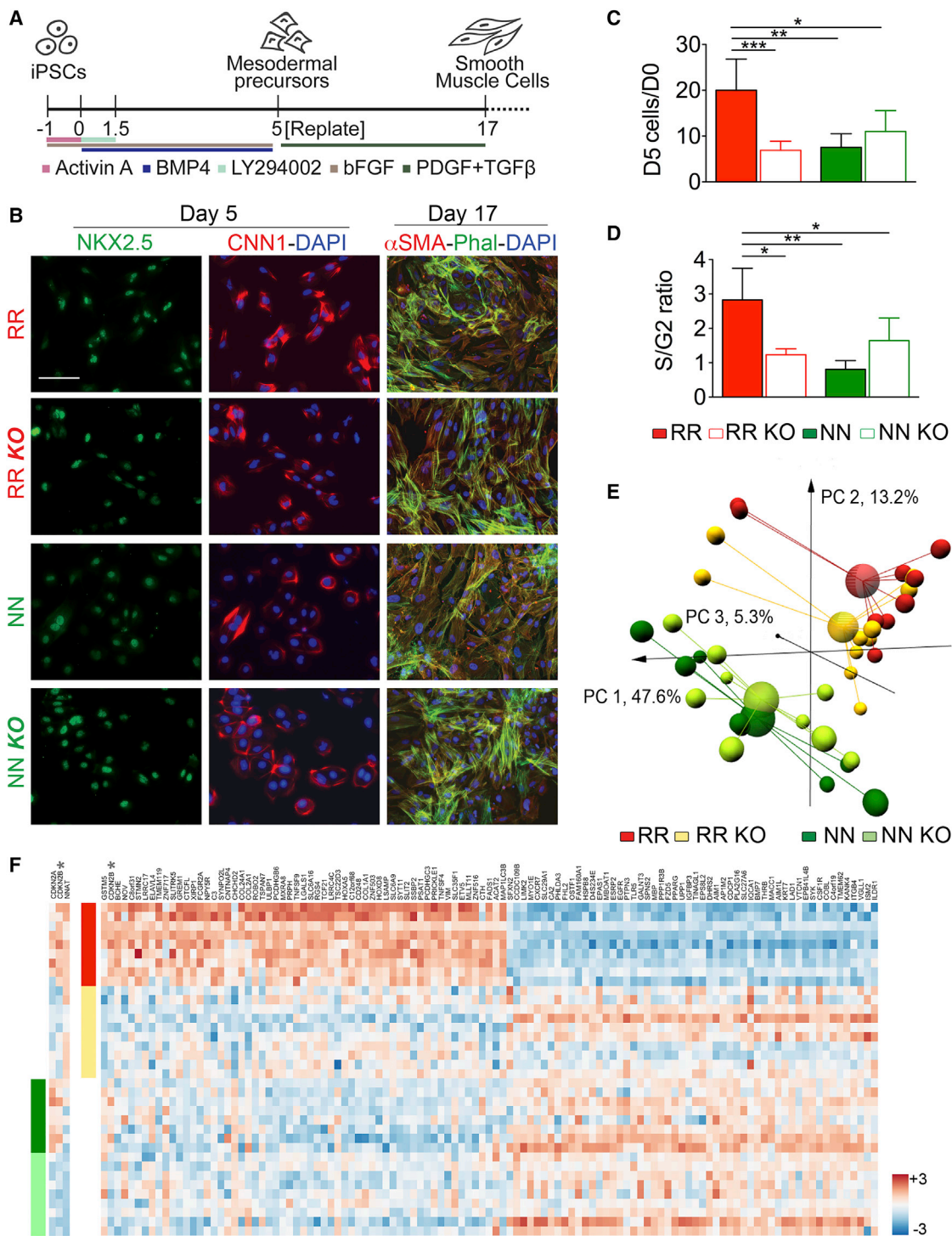
Figure 2. Differentiation of 9p21 KO hiPSCs into Vascular Smooth Muscle Cells and Effect of Deletion on Mesodermal Progenitors

(A) VSMC differentiation protocol for hiPSCs.

(B) Immunocytochemistry of VSMC differentiation. Cells stained for NKX2.5 and CNN1-DAPI at day 5 (D5) and α-SMA-Phalloidin-DAPI at D17. Scale bar, 100 μm.

(C) Cell count at D5 for the 4 different genotypes. The bar graph shows mean ± 95% CI of three independent experiments. For each experiment, 2–3 lines were used per genotype. *p < 0.05; **p < 0.001: ***p < 0.0001 one-way ANOVA-Bonferroni.

(D) DNA content analysis at D5 performed by propidium iodide staining followed by cytofluorimetric analysis. Graph shows the S/G2 ratio. Scale bar is mean ± SD. *p < 0.05, *p < 0.01 one-way ANOVA-Bonferroni.

(legend continued on next page)

The 9p21.3 Risk Haplotypes Differentially Affect VSMC Precursors

Next, we optimized an established method to differentiate VSMCs from iPSCs (Cheung et al., 2014). This method produces mesodermal progenitor-like cells (MP) that then can be induced to mature into VSMCs (Figure 2A). All iPSCs in the cohort produced MPs and VSMCs based on staining for key cell type markers (Figures 2B, S2A, and S2B). The haplotypes or their deletions did not impact differentiation, although we detected a small decrease in alpha-SMA+ cells in NN KO cells at day 17 (Figure S2A). In contrast, proliferation rates of the MPs were impacted by the 9p21.3 haplotype such that RR WT MPs proliferated more rapidly than NN cells. Unexpectedly, deleting the risk region in RR cells reverted their proliferation to that of NN WT MPs, while deleting the non-risk region in NN cells had no effect (Figures 2C, 2D, and S2A).

To evaluate the global impact of the 9p21.3 CVD locus, we performed an extensive set of RNA-seq experiments at three stages of differentiation for 14 different iPSC lines. To ensure consistency, multiple lines from each genotype were profiled in at least three independent biological experiments over the course of more than a year (Table S2). Principal component analyses (PCA) and clustering show that, as in the iPSCs, MP cells primarily cluster based on the donor, but suggest a trend in which the RR KO cells begin to resemble the NN and NN KO cells (Figures 2E and S2C). On day 3 of VSMC differentiation, deleting the 9p21.3 region in NN cells affected only three genes (Figure 2F). Of these genes, two are the neighboring *CDKN2B* and *CDKN2A* genes and the third is *NNAT*, which is an imprinted gene thought to be frequently misregulated in iPSCs.

In contrast, deleting the haplotype in RR cells resulted in differential expression of 113 genes (Figure 2F). This was surprising because the haplotypes differ by only 59–100 SNPs. These genes were linked to gene ontologies including developmental processes, system development, ectoderm development, and cell-cell adhesion (Figure 2F). Comparing the RR cells with the three other groups (RR KO, NN, and NN KO) identified 1,785 differentially expressed genes that are enriched in GO categories including embryo development, muscle development, and cell adhesion (Figure S2D; Table S3). While deletion of the risk or non-risk haplotypes both reduced *CDKN2B* expression, we did not detect differential expression of *CDKN2A* or *ANRIL* between the RR and NN cells.

The 9p21.3 Risk Haplotypes Differentially Impact Gene Expression in VSMCs

The gene expression differences in MP cells suggested that their more mature VSMC progeny might exhibit functional and transcriptional deficits that could shed light on CVD. Analyses of day 17 VSMCs revealed a striking difference between RR cells and RR KO cells (3,268 genes), while deletion of the NN region had only a modest effect (87 genes) (Figures 3A and S3A).

Remarkably, deletion of the RR haplotype restores the VSMCs to a transcriptional state resembling that of the NN and NN KO VSMCs, as shown by PCA (Figure 3B). The magnitude of this transcriptional change is on par with those seen between cells of different subtypes, suggesting that the risk locus may induce a cellular phenotypic switch, similar to those that VSMCs undergo in the vascular environment when inflammatory signals convert VSMCs from contractile cells to alternative fates, such as synthetic VSMCs (Alexander and Owens, 2012; Rensen et al., 2007; Bennett et al., 2016).

Analyses of this candidate gene regulatory network showed that the dysregulated genes are likely involved in cell cycle, DNA replication, and repair as previously reported (Figures 3C and S3B) (Motterle et al., 2012; Almontashiri et al., 2015), supporting the relevance of the model system. However, we also identified several novel candidate functional changes based on their enrichment in gene ontologies such as cell adhesion, muscle development, and muscle contraction (Figures 3C–3E; Table S3), which might also be expected to play roles in CAD. Mapping the differentially expressed genes to the genome showed that they are distributed across all chromosomes with no enrichment proximal to the 9p21 locus (Figure S3C), indicating that the risk haplotype in VSMCs can regulate genes in *trans*, either directly or indirectly.

VSMC Function Is Perturbed by the CVD Risk Haplotype

Guided by the RNA-seq analyses, we performed functional tests on sets of isogenic VSMCs using bioengineering and pharmacologic approaches. As predicted, mature RR VSMCs proliferated more quickly than NN VSMCs, while deleting the haplotype restored normal proliferation (Figure S3D). Next we measured VSMC contractile force using traction force microscopy (TFM) (Del Alamo et al., 2007) (Figure 4A), which quantifies the ability of cells to displace fluorescent beads embedded in a hydrogel. TFM showed that all cells maintained polarized traction forces (Figure 4B), but RR VSMCs exerted markedly lower traction forces than the three other genotypes (Figure 4C). Next, we quantified adhesion strength using a spinning disc assay in which cells are exposed to a range of stress forces depending on their radial position (Fuhrmann et al., 2014) (Figure 4D). RR cells exhibited weaker adhesion than NN cells with or without the deletion (Figure 4D). In both cases, deleting the RR locus restored normal function (Figures 4C and 4D).

In addition, we measured collective VSMC behavior in a collagen gel-based contraction assay that is compatible with pharmacologic studies. Again, the RR WT lines were outliers, exhibiting reduced contraction compared to the NN WT and NN KO lines. Deleting the risk haplotype restored contraction of the RR lines to levels of the NN lines (Figure 4E). These results could indicate that the RR cells are simply unhealthy or have lost the capacity to function as VSMCs. To test this, we employed pharmacologic agents that stimulate (bradykinin) or impair contraction (cytochalasin D) (Figure 4F). Bradykinin can restore gel contraction

---

(E) Principal component analysis (PCA) analysis of the whole transcriptome at D3.
(F) Heatmaps of genes differentially expressed (p-adj <0.05) between NN and its isogenic KO lines and RR and its isogenic KO lines. Legend of value is *Z* score. Details for number of samples used can be found in Table S2.
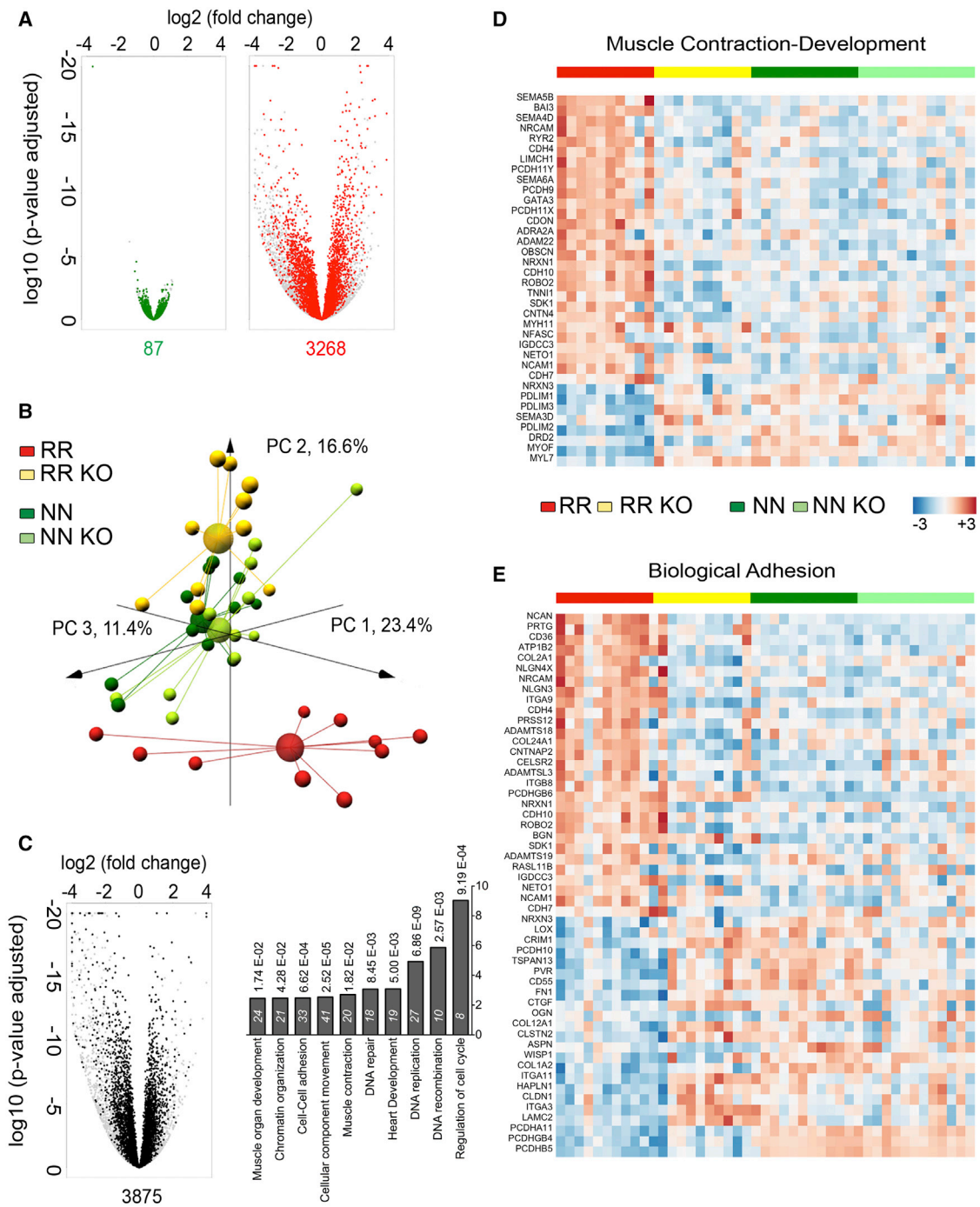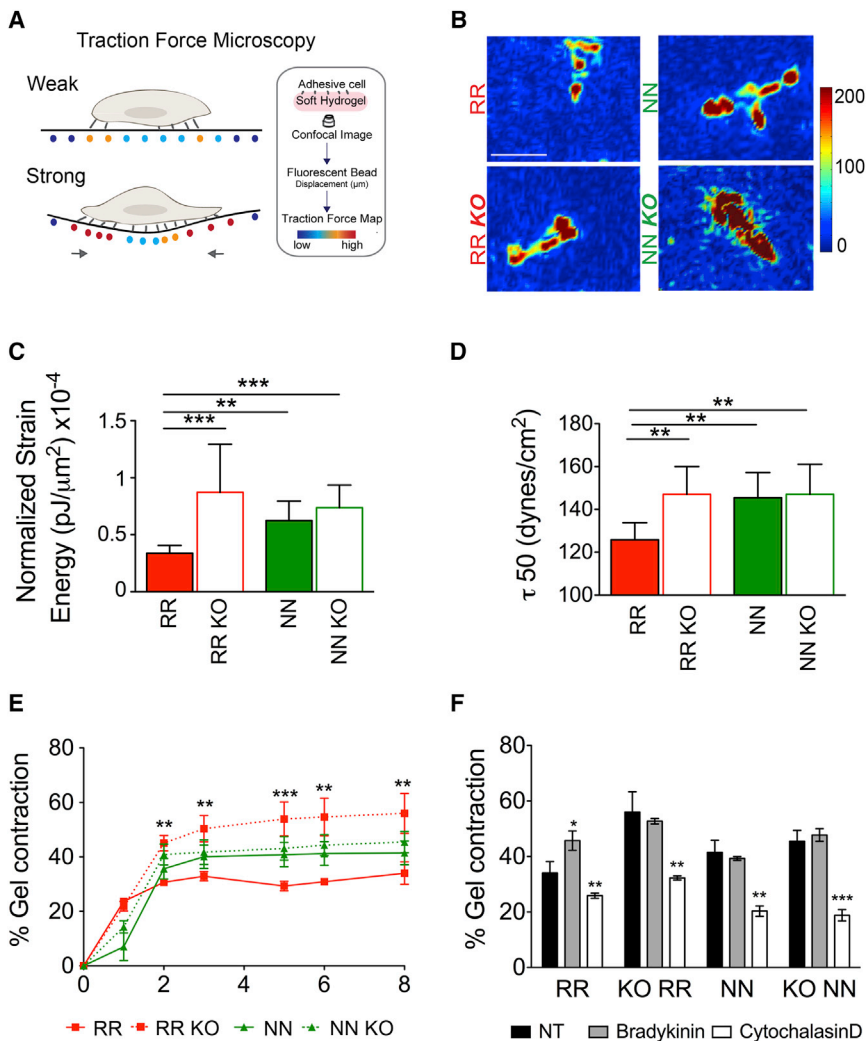See also Figure S2 and Table S3.

Figure 3. Effect of the 9p21 Risk Haplotype on VSMCs

(A) Volcano plots showing the significance versus fold change for all differentially expressed genes in VSMCs in a given comparison. Green, NN versus NN KO. Red, RR versus RR KO. Colored dots and numbers under the graphs show all genes differentially expressed that have counts greater than 100 in at least one of the samples; gray dots are those with lower levels of expression.

(B) PCA of D17 VSMCs. Spheres are different samples, larger spheres represent centroids of each set of samples.

(C) Left: volcano plot of the significance versus fold change for differentially expressed genes between RR and the other three cell groups (NN, NN KO, RR KO). Right: bar chart of GO term analysis of genes differentially expressed in RR VSMCs versus the other three groups. GO terms are listed based on fold enrichment, with the relative Bonferroni p value above, the number inside the column is number of genes differentially expressed in each term. GO categories with more than 2-fold enrichment are listed.

(legend continued on next page)

A Traction Force Microscopy

B

C

D

E

F

Figure 4. Functional Defects in VSMCs Carrying the 9p21.3 Risk Haplotype

(A) Traction force microscopy (TFM) assay.

(B) Tangential strain energy maps resulting from SMC traction forces on 11 kPa hydrogels. Representative heatmaps of each genotype shown. Scale bar, 50 μm.

(C) TFM assay: total strain energy normalized to cell area was plotted for VSMCs of varying genotypes (n > 25 in each assay; mean ± 95% CI). ***p < 0.001 one-way ANOVA-Bonferroni.

(D) Spinning disc assay for VSMCs of varying genotypes (n > 10 in each assay; mean ± 95% CI.). Each data point is a biological replicate derived from the τ_{50} of a sigmoidal fit of multiple technical replicates. **p < 0.01 one-way ANOVA-Bonferroni.

(E) Gel-based contraction assay during a time course of 8 days (mean ± SD). **p < 0.01, ***p < 0.001 one-way ANOVA each time point. Statistics represent RR lines versus RR KO. NN versus NN KO (ns).

(F) Gel-based contraction assay after pharmacological treatment with Bradykinin (10 nM) or cytochalasin D (0.5 μM). Plot shows data at D8 of treatment (mean ± SD). Statistics show one-way ANOVA-Bonferroni for NT versus bradykinin and NT versus cytochalasin D for each genotype, *p < 0.05, **p < 0.01, ***p < 0.001.

See also Figure S4 and Table S2.

capacity to RR WT VSMCs to a degree similar to NN, NN KO, or RR KO cells, indicating that they possess but do not use their contractile capabilities. Conversely depolymerization of the cytoskeleton with cytochalasin D significantly reduced contraction for all VSMCs. These analyses indicate that the RR cells maintain key functional properties of VSMCs, while exhibiting an altered cell state, and offer proof of principle that the effects of the risk locus can be reversed through pharmacologic intervention.

The Risk-Haplotype Alters *ANRIL* Expression

How might the risk haplotype induce the large transcriptional and functional phenotypic differences we observe in VSMCs? Although lacking known coding genes, the 9p21 risk interval contains the terminal exons of the lncRNA *ANRIL* (*CDKN2B-AS1*). Yet, none of the SNPs in this region fall into exons or

canonical splicing regions (Harismendy et al., 2011) (Figure 1A). Previous studies have uncovered extensive *ANRIL* alternative isoform usage, including circular isoforms, which can vary based on cell type, culture conditions, and/or the donor genetic background (Holdt et al., 2013, 2016; Holdt and Teupser, 2012; Hannou et al., 2015). Our isogenic lines and RNA-seq datasets provide a unique resource to assess *ANRIL* isoform expression levels in a particular cell type or lineage, under controlled culture conditions.

While previous studies used PCR across various exons to measure *ANRIL* levels, here, we made use of the RNA-seq data to perform an unbiased analysis of potential splice junctions found in day 17 VSMCs. This identified a set of predicted *ANRIL* junctions, leading to several candidate isoforms for each group of VSMCs (Figures 5A, S4A, and S4B). These alignments indicate that *ANRIL* isoform usage differs between the RR and NN lines. Specifically, in RR cells we observed enhanced splicing to an alternative terminating exon (13) that results in production of short *ANRIL* isoforms, while no splicing to exon 13 was detected in NN cells. In contrast, both NN and RR VSMCs exhibited splicing to the alternative terminal exon 19, which is found in

---

(D and E) Heatmaps showing differentially expressed (fold change >2) genes from GO term categories shown in (C).

(D) Heatmap includes genes present in the following categories: heart development, muscle contraction, and muscle organ development.

(E) Heatmap shows genes differentially expressed in the biological adhesion category. Values are *Z* score.
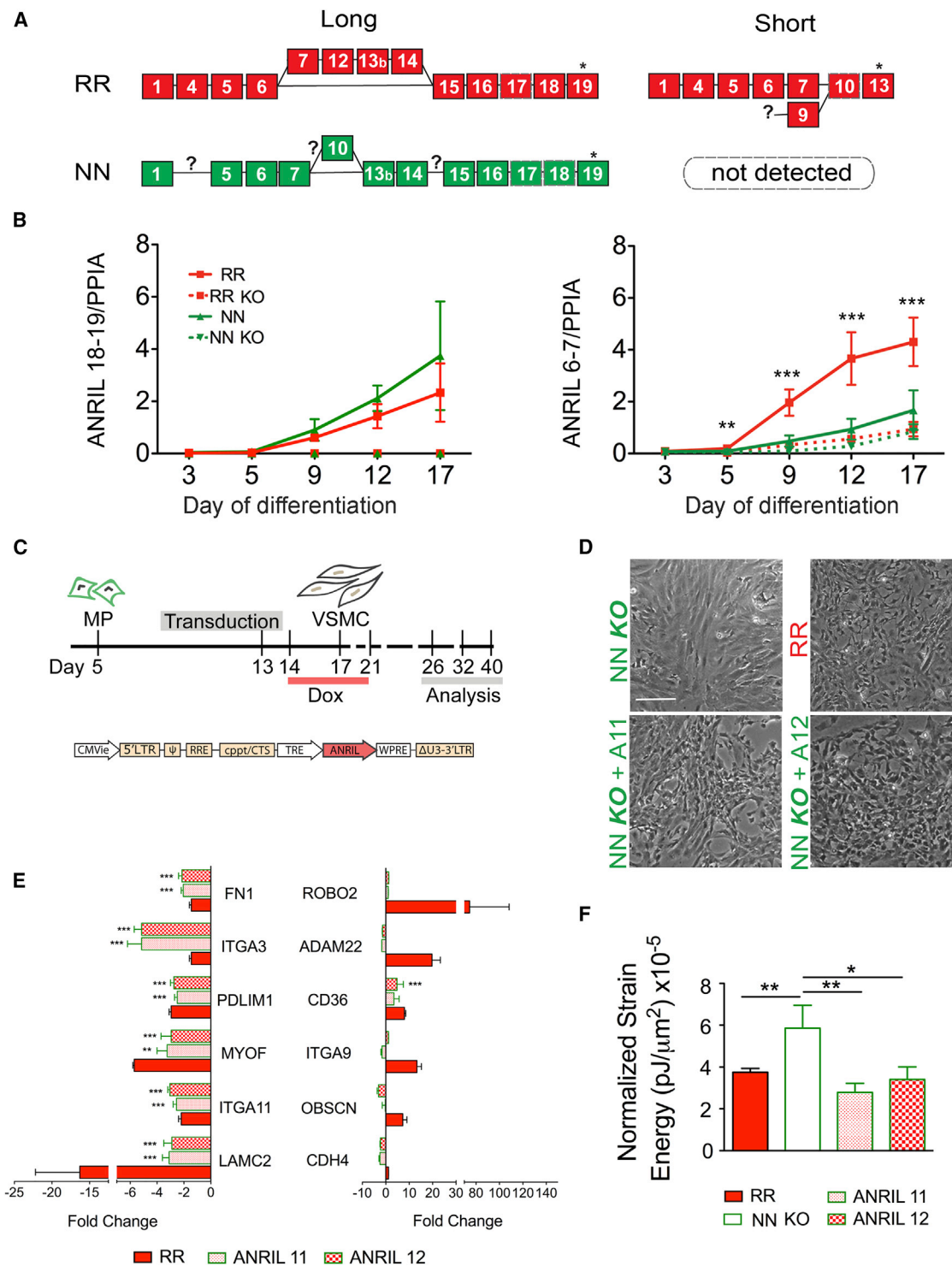
See also Figure S3 and Tables S2, S3, and S6.

Figure 5. Differential Expression of *ANRIL* isoforms in 9p21 RR VSMCs

(A) Schematic of predicted short (terminating in exon 13) and long (terminating in exon 19) *ANRIL* isoforms based on mapping RNA-seq reads across exon junctions. *, indicates termination sites; ?, indicates putative junctions, not detected in RNA-seq reads.

(B) Time course qRT-PCR of *ANRIL* expression during VSMC differentiation. Graphs show expression level of *ANRIL* transcripts using primers spanning two different exon-exon junctions: 18–19 (left, long isoforms), 6–7 (right, short and long isoforms). *PPIA* was used as housekeeping gene. Graphs show mean ± 95% CI. **p < 0.001, ***p < 0.0001 one-way ANOVA-Bonferroni for each time point.

(legend continued on next page)

long *ANRIL* isoforms (Figures 5A, S4A, and S4B). We note that some of the splice junctions we observed have not previously been reported, highlighting the potential complexity and context dependence of *ANRIL* splicing. However, due to the relatively low coverage of the upstream exons, this analysis is not likely a complete description of *ANRIL* isoforms in VSMCs.

To address this question using a second method, we employed a reverse transcription (RT)-PCR approach using template switching which confirmed the presence of two previously described short isoforms (11 and 12), and also detected a long isoform resembling previously described isoform 2, although with some subtle differences (Figure S4C) (Hannou et al., 2015; Holdt et al., 2013). We note that due to low expression levels and the potential for PCR-based jackpotting, these studies are not expected to be quantitative. We were unable to detect any of the previously described circular *ANRIL* isoforms, using RNA-seq alignments, bioinformatics methods to detect circular RNAs (STAR Methods) or real-time PCR-based assays (Holdt et al., 2016).

Next, we performed qRT-PCR using primers designed to detect the long isoforms (exons 18–19). As expected, long isoform expression is absent in KO VSMCs (Figure 5B). Long *ANRIL* isoforms levels are very low in iPSCs but increase throughout VSMC differentiation and are similar in RR and NN cell lines. In contrast, exons found both in the short and long isoforms (exons 5–6 or 6–7) increase throughout differentiation, but are more highly expressed in RR VSMCs (Figures 5B and S4D). This suggests that short isoforms are selectively increasing, as predicted by the RNA-seq alignments. We also directly examined expression of short *ANRIL* isoforms containing exon 13, confirming that the RR cells express higher levels than NN cells (Figure S4D).

ANRIL Expression in Non-risk VSMCs Partly Recapitulates the RR Phenotype

These expression studies support a model in which presence of the risk haplotype leads to increased expression of short *ANRIL* isoforms in RR cells relative to NN cells when they are differentiated into VSMCs *in vitro*. To test the effect of short *ANRIL* expression, we cloned isoforms 11 and 12 into inducible lentiviral expression vectors and expressed them during VSMC differentiation of NN KO cells (Figures 5C and S4E). Expressing the short *ANRIL* isoforms induced morphologic changes in mature NN VSMCs, inducing them to closely resemble the RR cells (Figure 5D).

qRT-PCR analyses of the top 12 differentially expressed genes (between NN, NN KO, RR KO, and RR) that are involved in adhesion and contraction (based on GO term analyses) showed that expressing the exogenous short *ANRIL* isoforms in NN KO cells reduces expression of all six genes that are lower in RR VSMCs compared to NN VSMCs, consistent with these

isoforms promoting VSMC cell fate plasticity (Figure 5E). In contrast, *ANRIL* expression only increased levels of one of the six tested genes (*CD36*) that are elevated in RR VSMCs. However, this gene is of particular interest because it is an oxidized low density lipoprotein receptor with known relevance to atherosclerosis (Park, 2014). To determine whether short *ANRIL* expression can affect VSMC function, we performed single cell contraction assays using traction force microscopy (TFM). Strikingly, we show that misexpression of short *ANRIL* in mature NN VSMCs reverts their phenotype and reduces their capacity to exert contractile force, such that they resemble the RR cells (Figure 5F). These experiments delineate novel roles for *ANRIL* expression in controlling VSMC phenotypic diversity. However, the incomplete recapitulation of all gene expression changes suggests that the effect of the entire risk haplotype effect may encompass more than the effects of short *ANRIL* expression.

Confirming Key Phenotypes in iPSC Lines from Different Individuals

By constructing and analyzing a large test set of isogenic haplotype-edited iPSC lines, we uncovered an unexpected additive gain-of-function role for the 9p21 CVD risk haplotype in VSMCs. To confirm these findings in other individuals, we generated a replication set of iPSCs from five additional RR and NN individuals bringing the total number of genetically distinct donors to seven (4 independent RR individuals and 3 NN; Table S2). We also produced RR KO cells from an additional donor (Figure 6A; Table S2). Using these new lines, we performed VSMC differentiations and tested the cells using the TFM and spinning disk adhesion assays previously described (Figure 6B, n = 22 total iPSC lines). In all assays, we observed statistically significant risk haplotype-dependent differences in replication set. We also confirmed that deletion of the risk haplotype is sufficient to restore contractile and adhesive function to VSMCs from a second risk individual (Figure 6B).

We next examined *ANRIL* expression in the new lines. As before, qRT-PCR experiments detected higher expression of *ANRIL* exons 6–7 (found in all isoforms) compared to exons 18–19 (long isoforms only) in all RR lines compared to all NN lines (Figure 6C). The unbiased non-quantitative analyses of short *ANRIL* isoforms identified isoforms 11, 12, and 13 in RR lines, although at differing relative ratios in different amplifications of independently constructed libraries from the same RNA, likely due to the "jackpotting" effect known to arise in PCR-based analyses of limiting samples (Figure S5A). In the two of the NN lines, we detected no short isoforms, while in one of the two other NN lines, we detected isoforms 11, 12, and 13. However, we did not detect increased levels of exons 6–7 in this line in qRT-PCR assays (Figure 6C), suggesting that these products are present at

(C) NN KO cells were transduced with doxycycline-inducible lentiviral vectors containing *ANRIL*–isoform 11 or 12 at D13 of VSMC differentiation. Doxycycline induction was initiated at D14, and cells were analyzed after 4 passages in culture.

(D) Phase-contrast images of NN KO rtTA, RR, NN KO + *ANRIL* 11 or 12 at passage 4. Scale bar, 200 μm.

(E) Transcriptional changes in NN KO VSMC overexpressing *ANRIL* 11 and 12. Graphs show qRT-PCRs for a subset of genes included in cell adhesion and muscle development GO terms previously described. Graphs show genes downregulated (left) and upregulated (right) in RR VSMC. Data are fold-change compared to NN KO (mean ± SEM) (n = 2 each condition). **p < 0.01 ***p < 0.001 one-way ANOVA-Bonferroni.

(F) TFM assay for VSMCs of varying genotypes (n > 25; mean ± SEM). *p < 0.05, **p < 0.01 one-way ANOVA-Bonferroni.

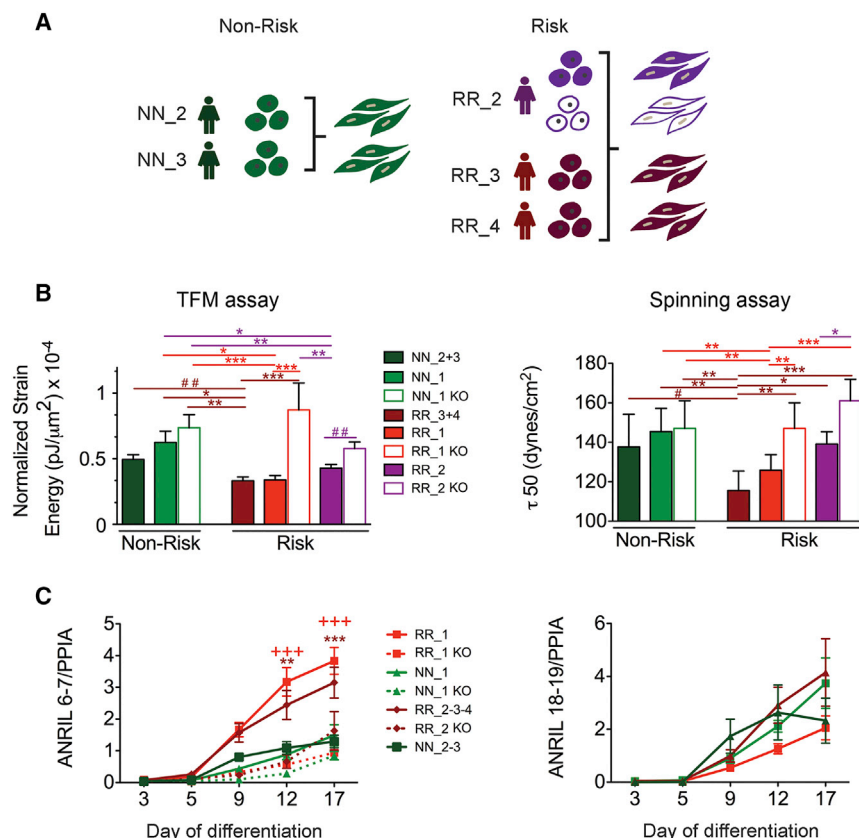See also Figures S4 and S5 and Table S2.

Figure 6. Risk-Dependent Phenotype Validation in iPSC-Derived VSMCs from Independent Individuals

(A) Schematic of additional iPSC generation and subsequent VSMC differentiation. 2 homozygous non risk (dark green) and 3 homozygous risk individuals were analyzed (purple and dark red). RR_2 (purple) iPSCs were further edited to generate KO iPSC lines.

(B) Left: TFM for VSMCs of different genotypes (n > 25; mean ± 95% CI). *p < 0.05, **p < 0.01, ***p < 0.0001 one-way ANOVA-Bonferroni, ##p < 0.01 unpaired t test. Right: spinning assay (n > 10; mean ± 95% CI). *p < 0.05, **p < 0.01, ***p < 0.0001 one-way ANOVA-Bonferroni, #p < 0.05 unpaired t test.

(C) ANRIL isoform expression in additional donors. Graphs show qRT-PCR of ANRIL isoforms containing exons 6–7 (left) and 18–19 (right). Bar is SEM. **p < 0.001 ***p < 0.0001 one-way ANOVA-Bonferroni for each time point.

See also Figures S5 and S6 and Table S2.

encompass 15 new risk loci (Howson et al., 2017). The expression patterns of the genes near these SNPs led the authors to propose a strong role for vascular wall cells, such as VSMCs in CVD genetic risk. Therefore, we examined the expression of these genes in our original isogenic RNA-seq dataset of haplotype-edited lines. Remarkably, 38 of the 91 of the genes associated with the 88 risk loci are dysregulated in VSMCs in the context of RR haplotype, which is a highly significant overlap (p = 0.0019, binomial distribution) (Figures 7A and 7B). Identifying this unexpected cell state and genotype-dependent transcriptional network of CAD risk genes that act in VSMCs represents a promising new avenue for clinical studies aimed at vascular wall-based mechanisms.

As the previous analysis shows, the large number of differentially expressed genes can constitute an important resource for understanding VSMC biology and CAD. To further explore gene networks regulated by the 9p21.3 risk haplotypes, we performed network analyses using ingenuity pathway analysis (IPA) and identified pathways affected by genes that differ between RR VSMCs and the other three genotypes (RR KO, NN, NN KO), using a control set of genes expressed at similar levels in these cells (Table S4) (Krämer et al., 2014). The most enriched pathways included Rho family GTPase signaling, integrin signaling, and actin cytoskeleton signaling, (Figures 7C and S6; Table S4), which are all pathways involved in de-differentiation of VSMCs. Many of these genes have also been previously implicated in CVD, based on the IPA Disease and Function Database (Figures 7C, S6B, and S6C). In contrast, only one canonical pathway was identified as enriched in the control gene set (PI3K/AKT signaling) (Table S4), providing evidence that the differentially expressed genes are relevant to specific aspects of VSMC function related to cell state and CAD.
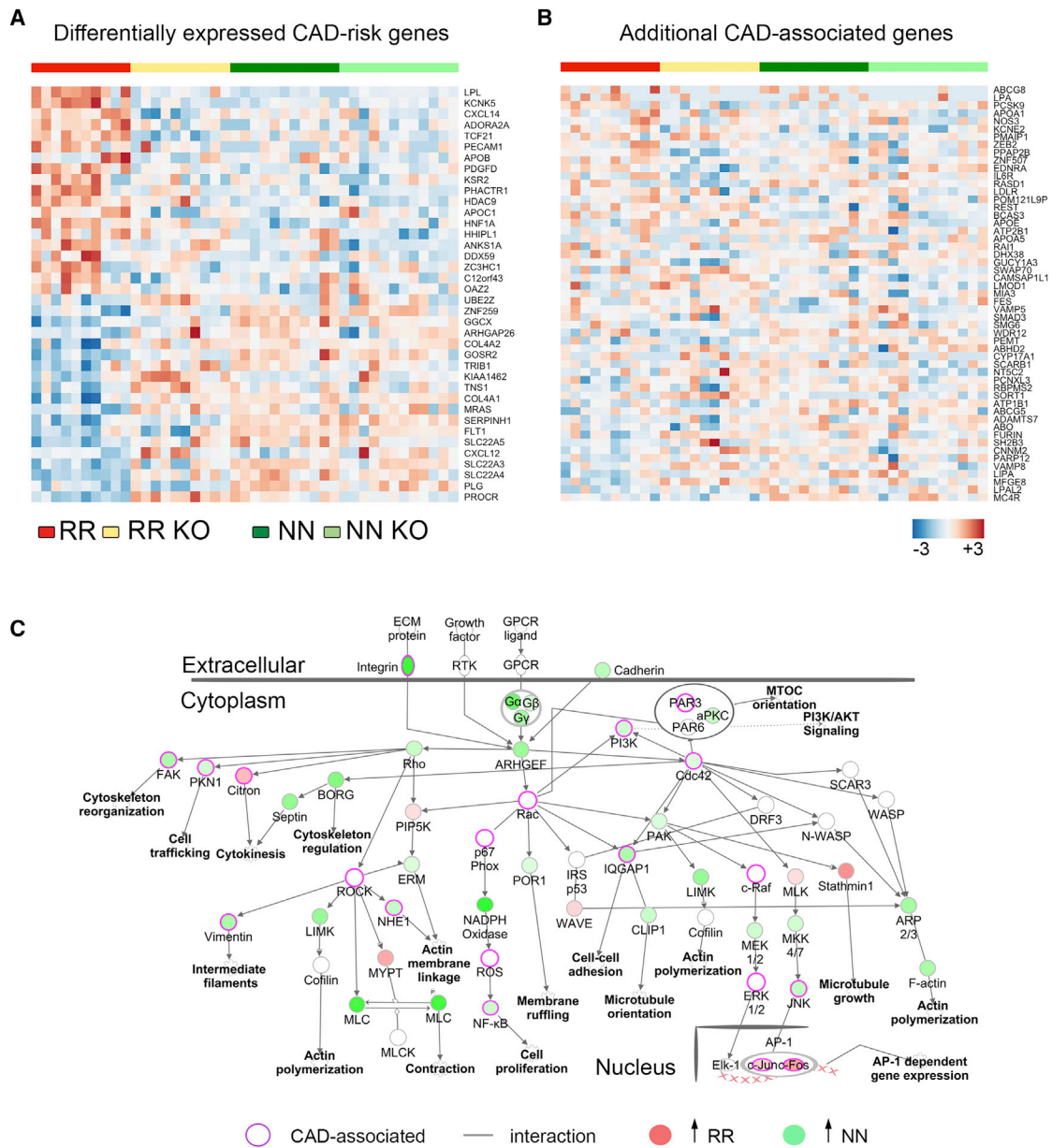
very low levels, consistent with our previous analyses of exon 13. We also detected several minor products that appeared to be novel ANRIL isoforms, though these could also be immature splicing forms or PCR-based artifacts. These studies highlight the potential complexity of ANRIL splicing as it relates to cell type.

Finally, we performed qRT-PCR analysis of eight genes related to adhesion and muscle contraction that we identified as the most significantly differentially expressed in RR versus NN VSMCs based on RNA-seq. These patterns of differential gene expression were consistent in the five new donor-derived iPSCs, with six meeting statistical significance and two (CD36 and ROBO2) exhibiting a trend that was not statistically significant (Figure S5B). Given the known heterogeneity in the behaviors of non-isogenic iPSCs (Carcamo-Orive et al., 2017; DeBoever et al., 2017), and known donor specific-effects on gene expression, these results support a strong and consistent role for risk haplotype status in governing the attributes of in vitro-derived VSMCs, acting partly through increased ANRIL expression.

9p21.3-Dependent Gene Networks Are Enriched in CVD Genes and Pathways

The mechanisms leading to increased risk for CVD can be inferred from genes identified in GWAS and other genomic studies. A recent large scale meta-analysis from the CARDIoGRAMplusC4D consortium (Nikpay et al., 2015) identified 73 independent loci associated with CVD, which have since been expanded to

Figure 7. Relevance for Cardiovascular Disease

(A and B) Heatmaps showing gene expression for 91 genes whose loci have been linked to CAD. Values are *Z* score. Heatmap in (A) shows statistically significant differentially expressed genes between RR and the other three genotypes. 38/91 genes are significantly different with a p = 0.0019 by binomial distribution. The 53 remaining genes are shown in (B).

(C) Canonical pathway analysis using Ingenuity Pathway Analysis. Rho GTPase signaling is shown.

See also Figures S6 and S7 and Tables S2, S4, and S6.

To link these pathways directly to effects on human vascular cells affected by CAD, we examined the results of a recent integrative genomics analysis of human coronary artery tissues derived from samples of affected individuals. This comprehensive study identified several key nodes of convergence for epigenetic and transcriptomic differences correlating with disease states with the strongest convergent node being AP1 signaling (Miller et al., 2016). The most significant IPA pathway related to

risk haplotype-dependent genes (Rho family GTPase signaling), also converges on AP1 signaling, directly linking the 9p21.3 regulated pathways to markers identified in diseased human arterial samples (Figure 7C). Other dysregulated genes such as *TCF21*, *PECAM1*, and *PDGFR* have previously been identified in GWAS studies and/or diseased human tissue (Miller et al., 2016).

IPA can also construct *de novo* networks based on lists of affected genes. We performed a *de novo* network analysis on

the set of genes differentially expressed in the RR cells versus NN and RR/NN KO cells, again using the control gene set for comparison. The networks derived from the differentially expressed gene list are enriched in genes related to CVD, cellular movement, cell morphology, cell-to-cell signaling, cellular compromise, cellular function, and maintenance and similar terms, while the control gene list networks were not (Figure S7; Table S5). Notably, some of the molecules in the network are also genes that we described previously as being directly altered by *ANRIL* overexpression in NN KO cells and which are known to play key roles in coronary artery disease (i.e., *CD36*, *LAMC2*, *FN1*, *ITGA3*). Together these analyses predict that gene expression differences in iPSC-derived VSMCs can be used to identify and understand gene expression networks related to disease in mature arterial wall cell types *in vivo* and, also, unexpectedly, link genes identified in association studies into transcriptional networks that appear to correlate with distinct VSMC states.

DISCUSSION

Human population genomic studies frequently identify genomic risk regions that are difficult to study due to a lack of coding SNPs, large blocks of linkage disequilibrium that prevent statistical disentanglement of linked variants, and/or inherent difficulties in modeling subtle genetic differences between humans with animal models. Here, we provide proof-of-principle that it is feasible to interrogate the function of these regions by performing homozygous deletion of large blocks of the human genome in iPSCs. This strategy offers advantages over analyses of large numbers of human primary cells derived from people of widely varying medical histories, ages, and genetic backgrounds as it significantly reduces most sources of background variation. This, in turn, increases the sensitivity of the assays, enabling comprehensive discovery of genetic changes driven by the risk haplotype. Indeed, the number of differentially regulated genes we have uncovered (~3,000) (Table S6) is significantly greater than those reported using gene chip-based profiling of human cell lines (~200–700) (Holdt et al., 2013). In addition, the expression differences we identify are large enough to detect significant enrichments in known CVD-related pathways and gene networks. As such, this study establishes the power of haplotype-edited iPSCs to identify the functional consequence of genetic variation in defined human cell types.

A second key advantage of the study design is the use of an independent replication set of iPSCs to confirm the key cellular and transcriptional phenotypes we observed in the initial test set. Importantly, we were able to demonstrate statistically significant haplotype-dependent differences in each assay we performed. This predicts that the effects of the haplotype may be robust and not strongly influenced by common genetic variation, though additional larger scale studies are needed to confirm this. Furthermore, unlike genetic variants that influence the expression of only a single gene and therefore have many potential genetic sources of subtle variation, the 9p21.3 haplotype-dependent effects encompass a very large network of genes and pathways for which we have demonstrated functional relevance.

Mechanisms Linking 9p21.3 Haplotypes to Cellular State Changes

How might the relatively small number of single nucleotide changes between the major 9p21.3 haplotypes (~59–100 SNPs in a ~60 kb region) lead to such a drastic cellular phenotypic switch in VSMCs, while having no significant impact on iPSCs? Intersecting our dataset with several recent integrative genomics and epigenomic studies suggest an attractive model. Our data suggest that the risk haplotype may contain SNPs that alter the function of enhancers that increase *ANRIL* expression (compared to the non-risk haplotype) because deleting the risk (but not non-risk) haplotype (*ANRIL* exons 10–19) reduces expression of the remaining upstream *ANRIL* exons (1–9) (Figure 5). Intriguingly, a recent paper examining long-range chromatin interactions showed that non-coding candidate regulatory regions within the 9p21.3 risk haplotype associated more strongly with the *ANRIL* enhancer (and also with the nearby *CDKN2B* enhancer) compared to the analogous region in the non-risk haplotype (Mumbach et al., 2017). This mechanism could explain at least part of the phenotype we observe, since we can mimic several key cellular and molecular phenotypes in NN KO cells via *ANRIL* overexpression. The failure of *ANRIL* overexpression to fully recapitulate the RR phenotype in NN KO cells is consistent with the possibility that additional variation in the 9p21.3 risk region may also influence cellular function, perhaps through additional enhancer regions, although this may also be due to technical issues.

The design of this study provides both correlative and causative evidence for the role of *ANRIL* in VSMCs and their mesodermal precursors. As *ANRIL* expression increases during iPSC to VSMC differentiation, the magnitude of the transcriptional shift grows. This suggests a causal role for *ANRIL* expression, which we confirm in NN KO cells through overexpression. These observations immediately pose the question of how increased *ANRIL* expression might trigger the global transcriptional changes we observe. One possibility, suggested by previous studies (Hannou et al., 2015), is that *ANRIL* expression, acting in *cis*, represses the *CDKN2B/A* genes, thereby inducing proliferation that, in turn, leads to a cellular phenotypic switch. However, our data are not fully consistent with this model because we observe lower *CNDKN2B* levels in NNKO and RRKO cells compared to NN cells, yet they have the similar proliferative phenotypes. We can also switch the phenotype of mature NN VSMCs through overexpression of *ANRIL* isoforms. Therefore, our data support a direct role variation at the risk locus and/or *ANRIL* in globally regulating gene expression and cellular function.

A second possibility is that, as reported previously, *ANRIL* interacts with polycomb group proteins (Devaux et al., 2015). While in previous studies, this interaction was reported only for genes in the vicinity of *ANRIL*, it remains possible that these interactions could act more broadly throughout the genome, or that *cis* interactions could trigger a more global transcriptional cascade resulting in the changed expression of ~3,000 genes. A third model could rely on the known capacity of long non-coding RNAs to act as sinks for regulatory microRNAs (Xu and Zhang, 2017). Future studies will be required to test these and other possible models.

Links to Cardiovascular Disease Mechanisms

While production of iPSC-derived VSMCs *in vitro* is unlikely to precisely mimic the events involved in CAD onset and progression, the cellular phenotypes we observe suggest an attractive model to explain how the 9p21.3 risk haplotype might influence CAD, stroke, or associated aneurysms through its action in VSMCs. In CAD, VSMCs are known to de-differentiate into a less contractile, less adhesive, and more motile cell state, termed the synthetic phenotype, which itself encompasses several functionally diverse cell states (Alexander and Owens, 2012; Rensen et al., 2007), CAD is also accompanied by the accumulation of inflammatory foam cells in atherosclerotic plaques (Libby et al., 2011). Intriguingly, although foam cells were traditionally thought to be derived from macrophages, lineage tracing studies in mice have shown that VSMCs can serve as a major source of foam cells (Alexander and Owens, 2012; Shankman et al., 2015) suggesting that VSMC cell fate plasticity could underlie CAD.

Here, we show that iPSC-derived human VSMCs carrying the risk haplotype exhibit several phenotypes consistent with this model. The RR VSMCs exhibit a large set of global changes to the cellular transcriptome that correlate with increased proliferation and decreased adhesion and contractile force in mature VSMC-like cells. Reduced VSMC adhesion and contraction as a result of the 9p21 risk haplotype may also be a reasonable explanation for concurrent increased risk for abdominal aortic and intracranial aneurysms, all which involve arterial wall regions that are under high shear stress. Finally, the datasets we have generated through comprehensive genome-wide transcriptomic profiling of this large set of haplotype-edited isogenic iPSCs supply a set of candidate targets and CAD-relevant pathways and mechanisms that may be explored in broader patient populations and clinical settings.

STAR★METHODS

Detailed methods are provided in the online version of this paper and include the following:

- KEY RESOURCES TABLE
- CONTACT FOR REAGENT AND RESOURCE SHARING
- EXPERIMENTAL MODEL AND SUBJECT DETAILS
  - Human Subjects
  - Cell lines
- METHOD DETAILS
  - Peripheral blood mononuclear cell isolation and culture
  - PBMC reprogramming to iPSCs
  - Induced pluripotent stem cells culture and characterization
  - Genome editing, transfection, genotyping
  - Smooth Muscle Cell Differentiation
  - RNA extraction and qRT-PCR
  - Library Preparation for RNA sequencing
  - *ANRIL* isoform amplification using template switching
  - ANRIL isoform overexpression
  - Deep sequencing and analysis of CAD Risk region
  - RNA-seq data analysis
  - Methods for detection of circular RNA from RNA-seq datasets

- Ingenuity Pathway Analysis
- Immunocytochemistry
- DNA content Analysis
- Cell Adhesion Strength Assay
- Traction Force Microscopy
- Gel Contraction Assay
- QUANTIFICATION AND STATISTICAL ANALYSIS
  - Statistical analysis
- DATA AND SOFTWARE AVAILABILITY

AUTHOR CONTRIBUTIONS

K.K.B., A.T., F.U., A.J.E., and E.J.T. conceived of various aspects of the project. V.L.S. and W.F. generated iPSC lines from PBMCs, performed gene editing, and SMC differentiation. F.U., L.Z., and G.C., designed TALE nucleases. V.L.S. performed DNA content analysis with help of M.D. V.L.S. and P.C. analyzed RNA-seq data with input from A.T. K.K.B., V.L.S., and P.C. performed ANRIL transcript analyses. P.C. performed ANRIL isoform specific RACE capture and ANRIL overexpression. A.K. and E.L.T. performed functional assays for adhesion and contraction. Experiments were designed and the manuscript was written by V.L.S., K.K.B., A.T., E.J.T., and A.J.E with input from the other authors.

REFERENCES

Alexander, M.R., and Owens, G.K. (2012). Epigenetic control of smooth muscle cell differentiation and phenotypic switching in vascular development and disease. Annu. Rev. Physiol. *74*, 13–40.

Almontashiri, N.A., Antoine, D., Zhou, X., Vilmundarson, R.O., Zhang, S.X., Hao, K.N., Chen, H.H., and Stewart, A.F. (2015). 9p21.3 Coronary artery disease risk variants disrupt TEAD transcription factor-dependent transforming growth factor β regulation of p16 expression in human aortic smooth muscle cells. Circulation *132*, 1969–1978.

Anders, S., Pyl, P.T., and Huber, W. (2015). HTSeq - a Python framework to work with high-throughput sequencing data. Bioinformatics *31*, 166–169.

Bennett, M.R., Sinha, S., and Owens, G.K. (2016). Vascular smooth muscle cells in atherosclerosis. Circ. Res. *118*, 692–702.

Bolger, A.M., Lohse, M., and Usadel, B. (2014). Trimmomatic: a flexible trimmer for Illumina sequence data. Bioinformatics *30*, 2114–2120.

Burton, P.R., Clayton, D.G., Cardon, L.R., Craddock, N., Duncanson, A., Kwiatkowski, D.P., McCarthy, M.I., Ouwehand, W.H., Todd, J.A., Donnelly, P., et al.; Wellcome Trust Case Control Consortium (2007). Genome-wide association study of 14,000 cases of seven common diseases and 3,000 shared controls. Nature *447*, 661–678.

Carcamo-Orive, I., Hoffman, G.E., Cundiff, P., Beckmann, N.D., D'Souza, S.L., Knowles, J.W., Patel, A., Papatsenko, D., Abbasi, F., Reaven, G.M., et al. (2017). Analysis of transcriptional variability in a large human iPSC library reveals genetic and non-genetic determinants of heterogeneity. Cell Stem Cell *20*, 518–532.

Carroll, D. (2014). Genome engineering with targetable nucleases. Annu. Rev. Biochem. *83*, 409–439.

Chen, H.-H., Almontashiri, N.A.M., Antoine, D., and Stewart, A.F.R. (2014). Functional genomics of the 9p21.3 locus for atherosclerosis: clarity or confusion? Curr. Cardiol. Rep. *16*, 502–508.

Cheung, C., Bernardo, A.S., Pedersen, R.A., and Sinha, S. (2014). Directed differentiation of embryonic origin-specific vascular smooth muscle subtypes from human pluripotent stem cells. Nat. Protoc. *9*, 929–938.

DeBoever, C., Li, H., Jakubosky, D., Benaglio, P., Reyna, J., Olson, K.M., Huang, H., Biggs, W., Sandoval, E., D'Antonio, M., et al. (2017). Large-scale profiling reveals the influence of genetic variation on gene expression in human induced pluripotent stem cells. Cell Stem Cell *20*, 533–546.

Del Alamo, J.C., Meili, R., Alonso-Latorre, B., Rodríguez-Rodríguez, J., Aliseda, A., Firtel, R.A., and Lasheras, J.C. (2007). Spatio-temporal analysis of eukaryotic cell motility by improved force cytometry. Proc. Natl. Acad. Sci. USA *104*, 13343–13348.

Devaux, Y., Zangrando, J., Schroen, B., Creemers, E.E., Pedrazzini, T., Chang, C.-P., Dorn, G.W., Thum, T., and Heymans, S.; Cardiolinc Network (2015). Long noncoding RNAs in cardiac development and ageing. Nat. Rev. Cardiol. *12*, 415–425.

Dichgans, M., Malik, R., König, I.R., Rosand, J., Clarke, R., Gretarsdottir, S., Thorleifsson, G., Mitchell, B.D., Assimes, T.L., Levi, C., et al.; METASTROKE Consortium; CARDIoGRAM Consortium; C4D Consortium; International Stroke Genetics Consortium (2014). Shared genetic susceptibility to ischemic stroke and coronary artery disease: a genome-wide analysis of common variants. Stroke *45*, 24–36.

Dobin, A., Davis, C.A., Schlesinger, F., Drenkow, J., Zaleski, C., Jha, S., Batut, P., Chaisson, M., and Gingeras, T.R. (2013). STAR: ultrafast universal RNA-seq aligner. Bioinformatics *29*, 15–21.

Doyon, Y., Vo, T.D., Mendel, M.C., Greenberg, S.G., Wang, J., Xia, D.F., Miller, J.C., Urnov, F.D., Gregory, P.D., and Holmes, M.C. (2011). Enhancing zinc-finger-nuclease activity with improved obligate heterodimeric architectures. Nat. Methods *8*, 74–79.

Fuhrmann, A., Li, J., Chien, S., and Engler, A.J. (2014). Cation type specific cell remodeling regulates attachment strength. PLoS ONE *9*, e102424.

García, A.J., Ducheyne, P., and Boettiger, D. (1997). Quantification of cell adhesion using a spinning disc device and application to surface-reactive materials. Biomaterials *18*, 1091–1098.

Go, W.Y., and Ho, S.N. (2002). Optimization and direct comparison of the dimerizer and reverse tet transcriptional control systems. J. Gene Med *4*, 258–270.

Gränsbo, K., Almgren, P., Sjögren, M., Smith, J.G., Engström, G., Hedblad, B., and Melander, O. (2013). Chromosome 9p21 genetic variation explains 13% of cardiovascular disease incidence but does not improve risk prediction. J. Intern. Med. *274*, 233–240.

Gschwendtner, A., Bevan, S., Cole, J.W., Plourde, A., Matarin, M., Ross-Adams, H., Meitinger, T., Wichmann, E., Mitchell, B.D., Furie, K., et al.; International Stroke Genetics Consortium (2009). Sequence variants on chromosome 9p21.3 confer risk for atherosclerotic stroke. Ann. Neurol. *65*, 531–539.

Guschin, D.Y., Waite, A.J., Katibah, G.E., Miller, J.C., Holmes, M.C., and Rebar, E.J. (2010). A rapid and general assay for monitoring endogenous gene modification. Methods Mol. Biol. *649*, 247–256.

Hannou, S.A., Wouters, K., Paumelle, R., and Staels, B. (2015). Functional genomics of the CDKN2A/B locus in cardiovascular and metabolic disease: what have we learned from GWASs? Trends Endocrinol. Metab. *26*, 176–184.

Harismendy, O., Notani, D., Song, X., Rahim, N.G., Tanasa, B., Heintzman, N., Ren, B., Fu, X.-D., Topol, E.J., Rosenfeld, M.G., and Frazer, K.A. (2011). 9p21 DNA variants associated with coronary artery disease impair interferon-γ signalling response. Nature *470*, 264–268.

He, S., Gu, W., Li, Y., and Zhu, H. (2013). ANRIL/CDKN2B-AS shows two-stage clade-specific evolution and becomes conserved after transposon insertions in simians. BMC Evol. Biol. *13*, 247.

Helgadottir, A., Thorleifsson, G., Manolescu, A., Gretarsdottir, S., Blondal, T., Jonasdottir, A., Jonasdottir, A., Sigurdsson, A., Baker, A., Palsson, A., et al. (2007). A common variant on chromosome 9p21 affects the risk of myocardial infarction. Science *316*, 1491–1493.

Helgadottir, A., Thorleifsson, G., Magnusson, K.P., Grétarsdóttir, S., Steinthorsdottir, V., Manolescu, A., Jones, G.T., Rinkel, G.J.E., Blankensteijn, J.D., Ronkainen, A., et al. (2008). The same sequence variant on 9p21 associates with myocardial infarction, abdominal aortic aneurysm and intracranial aneurysm. Nat. Genet. *40*, 217–224.

Holdt, L.M., and Teupser, D. (2012). Recent studies of the human chromosome 9p21 locus, which is associated with atherosclerosis in human populations. Arterioscler. Thromb. Vasc. Biol. *32*, 196–206.

Holdt, L.M., Beutner, F., Scholz, M., Gielen, S., Gäbel, G., Bergert, H., Schuler, G., Thiery, J., and Teupser, D. (2010). ANRIL expression is associated with atherosclerosis risk at chromosome 9p21. Arterioscler. Thromb. Vasc. Biol. *30*, 620–627.

Holdt, L.M., Sass, K., Gäbel, G., Bergert, H., Thiery, J., and Teupser, D. (2011). Expression of Chr9p21 genes CDKN2B (p15(INK4b)), CDKN2A (p16(INK4a), p14(ARF)) and MTAP in human atherosclerotic plaque. Atherosclerosis *214*, 264–270.

Holdt, L.M., Hoffmann, S., Sass, K., Langenberger, D., Scholz, M., Krohn, K., Finstermeier, K., Stahringer, A., Wilfert, W., Beutner, F., et al. (2013). Alu elements in ANRIL non-coding RNA at chromosome 9p21 modulate atherogenic cell functions through trans-regulation of gene networks. PLoS Genet. *9*, e1003588.

Holdt, L.M., Stahringer, A., Sass, K., Pichler, G., Kulak, N.A., Wilfert, W., Kohlmaier, A., Herbst, A., Northoff, B.H., Nicolaou, A., et al. (2016). Circular non-coding RNA ANRIL modulates ribosomal RNA maturation and atherosclerosis in humans. Nat. Commun. *7*, 12429.

Howson, J.M.M., Zhao, W., Barnes, D.R., Ho, W.-K., Young, R., Paul, D.S., Waite, L.L., Freitag, D.F., Fauman, E.B., Salfati, E.L., et al.; CARDIoGRAMplusC4D; EPIC-CVD (2017). Fifteen new risk loci for coronary artery disease highlight arterial-wall-specific mechanisms. Nat. Genet. *49*, 1113–1119.

Huang, W., Sherman, B.T., and Lempicki, R.A. (2009a). Bioinformatics enrichment tools: paths toward the comprehensive functional analysis of large gene lists. Nucleic Acids Res. *37*, 1–13.

Huang, W., Sherman, B.T., and Lempicki, R.A. (2009b). Systematic and integrative analysis of large gene lists using DAVID bioinformatics resources. Nat. Protoc. *4*, 44–57.

Jarinova, O., Stewart, A.F.R., Roberts, R., Wells, G., Lau, P., Naing, T., Buerki, C., McLean, B.W., Cook, R.C., Parker, J.S., and McPherson, R. (2009). Functional analysis of the chromosome 9p21.3 coronary artery disease risk locus. Arterioscler. Thromb. Vasc. Biol. *29*, 1671–1677.

Krämer, A., Green, J., Pollard, J., Jr., and Tugendreich, S. (2014). Causal analysis approaches in Ingenuity Pathway Analysis. Bioinformatics *30*, 523–530.

Lee, H.J., Kim, E., and Kim, J.-S. (2010). Targeted chromosomal deletions in human cells using zinc finger nucleases. Genome Res. *20*, 81–89.

Leek, J.T., Johnson, W.E., Parker, H.S., Jaffe, A.E., and Storey, J.D. (2012). The sva package for removing batch effects and other unwanted variation in high-throughput experiments. Bioinformatics 28, 882–883.

Li, H., Handsaker, B., Wysoker, A., Fennell, T., Ruan, J., Homer, N., Marth, G., Abecasis, G., and Durbin, R.; 1000 Genome Project Data Processing Subgroup (2009). The Sequence Alignment/Map format and SAMtools. Bioinformatics 25, 2078–2079.

Libby, P., Ridker, P.M., and Hansson, G.K. (2011). Progress and challenges in translating the biology of atherosclerosis. Nature 473, 317–325.

Liu, P.-Q., Chan, E.M., Cost, G.J., Zhang, L., Wang, J., Miller, J.C., Guschin, D.Y., Reik, A., Holmes, M.C., Mott, J.E., et al. (2010). Generation of a triple-gene knockout mammalian cell line using engineered zinc-finger nucleases. Biotechnol. Bioeng. 106, 97–105.

Liu, Y., Zheng, L., Wang, Q., and Hu, Y.-W. (2017). Emerging roles and mechanisms of long noncoding RNAs in atherosclerosis. Int. J. Cardiol. 228, 570–582.

Lo Sardo, V., Ferguson, W., Erikson, G.A., Topol, E.J., Baldwin, K.K., and Torkamani, A. (2017). Influence of donor age on induced pluripotent stem cells. Nat. Biotechnol. 35, 69–74.

Love, M.I., Huber, W., and Anders, S. (2014). Moderated estimation of fold change and dispersion for RNA-seq data with DESeq2. Genome Biol. 15, 550.

McPherson, R., and Tybjaerg-Hansen, A. (2016). Genetics of coronary artery disease. Circ. Res. 118, 564–578.

McPherson, R., Pertsemlidis, A., Kavaslar, N., Stewart, A., Roberts, R., Cox, D.R., Hinds, D.A., Pennacchio, L.A., Tybjaerg-Hansen, A., Folsom, A.R., et al. (2007). A common allele on chromosome 9 associated with coronary heart disease. Science 316, 1488–1491.

Mi, H., Muruganujan, A., Casagrande, J.T., and Thomas, P.D. (2013). Large-scale gene function analysis with the PANTHER classification system. Nat. Protoc. 8, 1551–1566.

Mi, H., Poudel, S., Muruganujan, A., Casagrande, J.T., and Thomas, P.D. (2016). PANTHER version 10: expanded protein families and functions, and analysis tools. Nucleic Acids Res. 44 (D1), D336–D342.

Miller, J.C., Tan, S., Qiao, G., Barlow, K.A., Wang, J., Xia, D.F., Meng, X., Paschon, D.E., Leung, E., Hinkley, S.J., et al. (2011). A TALE nuclease architecture for efficient genome editing. Nat. Biotechnol. 29, 143–148.

Miller, C.L., Pjanic, M., Wang, T., Nguyen, T., Cohain, A., Lee, J.D., Perisic, L., Hedin, U., Kundu, R.K., Majmudar, D., et al. (2016). Integrative functional genomics identifies regulatory mechanisms at coronary artery disease loci. Nat. Commun. 7, 12092.

Motterle, A., Pu, X., Wood, H., Xiao, Q., Gor, S., Ng, F.L., Chan, K., Cross, F., Shohreh, B., Poston, R.N., et al. (2012). Functional analyses of coronary artery disease associated variation on chromosome 9p21 in vascular smooth muscle cells. Hum. Mol. Genet. 21, 4021–4029.

Mumbach, M.R., Satpathy, A.T., Boyle, E.A., Dai, C., Gowen, B.G., Cho, S.W., Nguyen, M.L., Rubin, A.J., Granja, J.M., Kazane, K.R., et al. (2017). Enhancer connectome in primary human cells identifies target genes of disease-associated DNA elements. Nat. Genet. 49, 1602–1612.

Nikpay, M., Goel, A., Won, H.H., Hall, L.M., Willenborg, C., Kanoni, S., Saleheen, D., Kyriakou, T., Nelson, C.P., Hopewell, J.C., et al. (2015). A comprehensive 1,000 genomes-based genome-wide association meta-analysis of coronary artery disease. Nat. Genet. 47, 1121–1130.

Park, Y.M. (2014). CD36, a scavenger receptor implicated in atherosclerosis. Exp. Mol. Med. 46, e99.

Picelli, S., Faridani, O.R., Björklund, Å.K., Winberg, G., Sagasser, S., and Sandberg, R. (2014). Full-length RNA-seq from single cells using Smart-seq2. Nat. Protoc. 9, 171–181.

Rensen, S.S., Doevendans, P.A., and van Eys, G.J. (2007). Regulation and characteristics of vascular smooth muscle cell phenotypic diversity. Neth. Heart J. 15, 100–108.

Samani, N.J., Erdmann, J., Hall, A.S., Hengstenberg, C., Mangino, M., Mayer, B., Dixon, R.J., Meitinger, T., Braund, P., Wichmann, H.E., et al.; WTCCC and the Cardiogenics Consortium (2007). Genomewide association analysis of coronary artery disease. N. Engl. J. Med. 357, 443–453.

Shankman, L.S., Gomez, D., Cherepanova, O.A., Salmon, M., Alencar, G.F., Haskins, R.M., Swiatlowska, P., Newman, A.A.C., Greene, E.S., Straub, A.C., et al. (2015). KLF4-dependent phenotypic modulation of smooth muscle cells has a key role in atherosclerotic plaque pathogenesis. Nat. Med. 21, 628–637.

Shea, J., Agarwala, V., Philippakis, A.A., Maguire, J., Banks, E., Depristo, M., Thomson, B., Guiducci, C., Onofrio, R.C., Kathiresan, S., et al.; Myocardial Infarction Genetics Consortium (2011). Comparing strategies to fine-map the association of common SNPs at chromosome 9p21 with type 2 diabetes and myocardial infarction. Nat. Genet. 43, 801–805.

Thorvaldsdóttir, H., Robinson, J.T., and Mesirov, J.P. (2013). Integrative Genomics Viewer (IGV): high-performance genomics data visualization and exploration. Brief. Bioinform. 14, 178–192.

Visel, A., Zhu, Y., May, D., Afzal, V., Gong, E., Attanasio, C., Blow, M.J., Cohen, J.C., Rubin, E.M., and Pennacchio, L.A. (2010). Targeted deletion of the 9p21 non-coding coronary artery disease risk interval in mice. Nature 464, 409–412.

Wen, J.H., Vincent, L.G., Fuhrmann, A., Choi, Y.S., Hribar, K.C., Taylor-Weiner, H., Chen, S., and Engler, A.J. (2014). Interplay of matrix stiffness and protein tethering in stem cell differentiation. Nat. Mater. 13, 979–987.

Xu, F., and Zhang, J. (2017). Long non-coding RNA HOTAIR functions as miRNA sponge to promote the epithelial to mesenchymal transition in esophageal cancer. Biomed. Pharmacother. 90, 888–896.

STAR★METHODS

KEY RESOURCES TABLE

REAGENT or RESOURCE	SOURCE	IDENTIFIER
Antibodies		
anti-SSEA4 PE	Stemgent	Cat#09-0003; RRID: AB_1266951
anti-Tra-1-81	Millipore	Cat# MAB4381; RRID: AB_177638
anti-Tra-1-60	Millipore	Cat# MAB4360; RRID: AB_2119183
anti-Nanog	Abcam	Cat# AB21624; RRID: AB_446437
anti-Smooth Muscle Actin	Sigma	Cat# A5228; RRID: AB_262054
anti-Phalloidin Alexa 488	Life Tech	Cat# A12379; RRID: AB_2315147
anti-Nkx2.5	SCBT	Cat# SC-14033; RRID: AB_650281
anti-Transgelin	Abcam	Cat# AB14106; RRID: AB_443021
anti-Calponin1	Sigma	Cat# C2687; RRID: AB_476840
Goat anti-mouse-IgG Alexa 555	Invitrogen	Cat# A21426; RRID: AB_1500929
Goat anti-mouse-IgM Alexa 488	Invitrogen	Cat# A21426; RRID: AB_1500929
Goat anti-rabbit-IgG Alexa 488	Invitrogen	Cat# A11008; RRID: AB_143165
Goat anti-mouse-IgG Alexa 488	Invitrogen	Cat# A21042; RRID: AB_2535711
Donkey anti-mouse-IgG Alexa 555	Invitrogen	Cat# A31570; RRID: AB_2536180
Bacterial and Virus Strains		
One Shot TOP10 Chemically Competent *E. coli*	Invitrogen	Cat#C404010
NEB Stable	NEB	Cat#: C3040H
Biological Samples		
Inactivated human foreskin fibroblasts	EMD-Millipore	Cat# SCC057
Chemicals, Peptides, and Recombinant Proteins		
Ficoll-Paque Premium	GE Healthcare	Cat# 17-5442-03
Dulbecco's Phosphate Buffered Saline, +MgCl +CaCl	GIBCO	Cat# 14040133
Dulbecco's Phosphate Buffered Saline, -MgCl -CaCl	GIBCO	Cat# 14190136
Dimethyl Sulfoxide (DMSO)	Fisher	Cat# BP231100
Fetal bovine serum (PBMC cryo, iPSC characterization)	GIBCO	Cat# 10082139
Fetal bovine serum, Benchmark (10% FBS mediums)	Gemini	Cat# 100106
IMDM	GIBCO	Cat #21056023
Ham's F12	GIBCO	Cat# 31765035
Glutamax	GIBCO	Cat# 35050061
Chemically Defined Lipid Concentrate	GIBCO	Cat# 11905031
Insulin-Transferrin-Selenium-Ethanolamine (ITS -X)	GIBCO	Cat# 51500056
1-thioglycerol	Sigma	Cat# M6145
Bovine serum albumin	Sigma	Cat# A9418
Ascorbic acid	Sigma	Cat# A8960
rhEPO	R&D	Cat# 287-TC-500
hSCF	R&D	Cat# 255-SC-050
rhIGF1	R&D	Cat# 291-G1-200
hIL3	R&D	Cat# 203-IL-010
Dexamethasone	Sigma	Cat# D2915
Holo-transferrin	R&D	Cat# 2914-HT
Human CD34+ nucleofector kit	Lonza	Cat# VPA-1003
Human Stem Cell kit 1 nucleofector kit	Lonza	Cat# VPH-5012

(Continued on next page)

Continued

REAGENT or RESOURCE	SOURCE	IDENTIFIER
mTeSR1 medium	Stemcell Tech	Cat# 05850
Sodium butyrate	Alfa Aesar	Cat# A11079
Matrigel	Corning	Cat# 354277
Accutase	Innovative Cell Tech	Cat# AT-104
Y-27632 Dihydrochloride	Tocris	Cat# 1254
Ethylenediaminetetraacetic acid (EDTA)	Invitrogen	Cat# 15575020
Tris HCl	Sigma	Cat# T2194-1L
Sodium chloride	Sigma	Cat# S5150-1L
Sodium dodecyl sulfate	Sigma	Cat# 05030-500ML-F
Proteinase K	Roche	Cat# 03115828001
RNase A	QIAGEN	Cat# 1007885
mMESSAGE mMACHINE T7 ULTRA Transcription Kit	Ambion	Cat# AM1345
RNeasy Mini Kit	QIAGEN	Cat# 74104
Phenol/chloroform/isoamyl alcohol	Invitrogen	Cat# 15593031
Sodium acetate	Ambion	Cat# AM9740
Ethanol	Fisher	Cat# BP2818
Water, nuclease-free	Ambion	Cat# AM9932
TRIS EDTA buffer, pH 8	Ambion	Cat# AM9849
Trizol	Invitrogen	Cat# 15596
DNA-free	Ambion	Cat# AM1906
iScript cDNA Synthesis Kit	Bio-Rad	Cat# 1708891
iTaq Universal SyBr Green Supermix	Bio-Rad	Cat# 1725121
Ovation RNA-Seq System V2	Nugen	Cat# 7102
Agencourt Ampure XP beads	Beckman Coulter	Cat# A63882
Sure Select XT2 adapters	Agilent	Cat# G9621A
RNasin Plus Ribonuclease Inhibitors (Thermostable)	Promega	Cat# N2615
Maxima H- reverse transcriptase	Thermofisher	Cat# EP0751
KAPA HiFi ready mix	Kapabiosystems	Cat# KK2601
Bluepippin Prep	Sage Science	Cat# CDF1510
KAPA Hyper Prep kit	Kapabiosystems	Cat# KR0961
DMEM	GIBCO	Cat# 10566016
Penicillin/Streptomycin, used as 100x stock	GIBCO	Cat# 15140122
Non-essential amino acids (NEAA)	GIBCO	Cat# 11140050
TrypLE Express	GIBCO	Cat# 12604013
Gel DNA purification kit	Zymo	Cat# D4001
Q5 polymerase	NEB	Cat# M0491S
Buffer EB	QIAGEN	Cat# 1014612
PrimeStar GXL	Takara	Cat# R050A
LentiX Concentrator	Takara	Cat# 631232
Sodium pyruvate	GIBCO	Cat# 11360070
Doxycycline hyclate	Sigma	Cat# D9891-10G
Low-melt agarose	Bio-Rad	Cat# 161-3114
Agarase	NEB	Cat# M0392S
Isopropanol	Fisher	Cat# A4154
Nextera XT Library Preparation kit (Deep Seq)	Illumina	Cat# FC-131-1024
0.1% gelatin in ultrapure water	Millipore	Cat# ES-006-B
Paraformaldehyde	Electron Microscopy Sciences	Cat# 15710
DAPI nuclear stain	Life Tech	Cat# D1306

Continued

REAGENT or RESOURCE	SOURCE	IDENTIFIER
Propidium iodide	Sigma	Cat# P4864
Triton X-100	Sigma	T8787-250ML
0.1% gelatin in DI water (adhesion strength assay)	Stemcell Tech	Cat# 07903
Phosphate buffered saline with Mg & Ca	Cellgro	Cat# 20-030-CV
Dextrose	Fisher	Cat# BP350-1
Formaldehyde (adhesion strength assay)	Fisher	Cat# F79
Hoescht stain	Fisher	Cat# H3570
Fluoromount-G	Southern Biotech	Cat# 0100-01
UV/ozone generation	BioForce Nanosciences	Cat# 1062
3-(trimethoxysilyl)propyl methacrylate	Sigma	Cat# 440159
Acrylamide	Sigma	Cat# A4058
Bis-acrylamide	Fisher	Cat# BP1404
Ammonium persulfate	Fisher	Cat# BP179
N,N,N',N'-Tetramethylethylenediamine	VWR	Cat# IC805615
580/605 0.2um microspheres	Invitrogen	Cat# F8810
Dichlorodimethylsilane	Acros Organics	Cat# 430881000
N-sulphosuccinimidyl-6-(4'-azido-2'-nitrophenylamino) hexanoate	Fisher	Cat# 22589
HEPES	Spectrum Chemical	Cat# HE155
Trypsin	Fisher	Cat# 15090046
DMEM	Thermo	Cat# 12100061
Fetal Bovine Serum	Gemini Bio-Products	Cat# 900-108
Type-1 rat tail collagen	Corning	Cat# 354236
Bradykinin	Sigma	Cat# B3259
CytochalasinD	Sigma	Cat# C2618
Critical Commercial Assays		
Mycoplasma PCR Detection Kit	Sigma	Cat# MP0035
JumpStart TAQ DNA Polymerase (for Mycoplasma kit)	Sigma	Cat# D9307
Infinium HumanCoreExome BeadChip	Illumina	Cat# WG-330-1101
DNA 1000 LabChip (RNaseq quality control)	Agilent	Cat# 5065-1504
Deposited Data		
RNASeq data	This paper	GEO: GSE120099
Experimental Models: Cell Lines		
Human: LentiX HEK293T	Takara	Cat# 632180
Human: Patient PBMC-derived iPS cell lines	Lo Sardo et al., 2017	WiCell
Oligonucleotides		
GJC 344F (5' CATACAGGTCCCTGGCACTAA 3')	This paper	N/A
GJC 345R (5' GAGCCAACGATATCTCCAAGA 3')	This paper	N/A
GJC 346F (5' CGAAGGGCTTCCCTGTCTA 3')	This paper	N/A
GJC 347R (5' GACTTTCCCCCA CAATGAAA 3')	This paper	N/A
qPCR primers, see Table S4		N/A
SMARTseq2-(dT)$_{30}$ (5' AAGCAGTGGTATCAACGCA GAGTACT$_{30}$ 3')	Picelli et al., 2014	N/A
Template switch oligo (5'AAGCAGTGGTATCAACGCA GAGTACATrGrG+G 3')	Picelli et al., 2014	N/A
Recombinant DNA		
pCXLE-hOCT3/4-shp53		Addgene ID: 27077
pCXLE-hSK		Addgene ID: 27078

(Continued on next page)

Continued

REAGENT or RESOURCE	SOURCE	IDENTIFIER
pCXLE-hUL		Addgene ID: 27080
pTRE-A11-wPRE (Chubukov)	This paper	N/A
pTRE-A12-wPRE (Chubukov)	This paper	N/A
pMD2.G		Addgene ID: 12259
pRSV-Rev		Addgene ID: 12253
pMDLg/pRRE		Addgene ID: 12251
pFU-UbC-rtTA M2.2	Go and Ho, 2002	Mark Mayford laboratory, UCSD, La Jolla, CA
Software and Algorithms		
Trimmomatic PE v0.32	Bolger et al., 2014	RRID: SCR_011848
STAR aligner v2.3.0	Dobin et al., 2013	RRID: SCR_015899
HTseq	Anders et al., 2015	RRID: SCR_005514
DESeq2 R package (v1.8.2)	Love et al., 2014	RRID: SCR_015687
Samtools 1.3	Li et al., 2009	RRID: SCR_002105
Integrative Genomics Viewer 2.3.80	Thorvaldsdóttir et al., 2013	RRID: SCR_011793
Surrogate Variable Analysis v3.18.0	Leek et al., 2012	RRID: SCR_012836
gplots package	N/A	N/A
rgl R package		N/A
pca3d R package	N/A	N/A
Panther Classification System (v10.0, 2015-05-15)	Mi et al., 2013; 2016	RRID: SCR_004869
DAVID Bioinformatics Resources 6.7	Huang et al., 2009a; 2009b	RRID: SCR_003033
Ingenuity Pathway Analysis	QIAGEN	RRID: SCR_008653
Metamorph 7.6 (adhesion strength/traction force assays)	Molecular Devices	RRID: SCR_002368
MATLAB, custom scripts (adhesion strength/traction force assays)	Fuhrmann et al., 2014	RRID: SCR_001622
ImageJ	NIH	https://imagej.nih.gov/ij/
Other		
Patient-derived iPS cell lines	Lo Sardo et al., 2017	https://www.wicell.org/home/stem-cell-lines/catalog-of-stem-cell-lines/collections/nhlbi-next-gen-topol.cmsx

CONTACT FOR REAGENT AND RESOURCE SHARING

Further information and requests for resources and reagents should be directed to and will be fulfilled by the Lead Contact, Kristin K. Baldwin (kbaldwin@scripps.edu).

EXPERIMENTAL MODEL AND SUBJECT DETAILS

Human Subjects

Study participants were enrolled and informed consent obtained under study IRB-11-5676 approved by the Scripps Institutional Review Board. Peripheral blood mononuclear (PBMCs) cells obtained from patient blood samples were expanded and reprogrammed to establish multiple induced pluripotent stem cell (iPSC) lines for each patient. Cell lines included in this study were derived from the following donors: C00512 male, 57 yo (years old), referred in the manuscript as RR; HE00463 male, 86 yo, referred as NN; C0021 male 59 yo, (RR_2); HE787 male 87 yo (RR_3); C568 male 69 yo (RR_4); C939 male 92yo (NN_2); C664 male 79yo (NN_3). Genotype was determined by PCR for three common SNPs at 9p21.3: rs1333049, rs2383207, rs10757278.

Cell lines

The peripheral blood mononuclear cells (PBMC) fraction was isolated from peripheral blood by Ficoll-Paque density gradient separation and cryopreserved until later use.

HEK293T (human embryonic kidney) were obtained from Clontech. iPSC cell lines were derived by episomal reprogramming of PBMCs and generated in the Baldwin Laboratory (Lo Sardo et al., 2017). Some of the iPSC lines are available at WiCell in the NHLBI Next Gen - Coronary Artery Disease And Myocardial Infarction (Dr. Eric Topol, Scripps Research Institute) collection, at the following link: https://www.wicell.org/home/stem-cells/catalog-of-stem-cell-lines/collections/nhlbi-next-gen-topol.cmsx

The cell line numbers correspond to the following accession numbers in WiCell: C00512 (SCRP0517i), C568-1 (SCRP0601i), C664-9 (SCRP0709i). HE463 (SCRP2307i), HE787-3 (SCRP2503i), C939-2 (SCRP0802i).

METHOD DETAILS

Peripheral blood mononuclear cell isolation and culture

PBMC isolation from blood in Heparin vacutainers was performed using Ficoll-PaquePremium (GE Healthcare, cat #17-5442-03). Blood was diluted with 10 mL 1X PBS, layered over the top of 20 mL Ficoll and then centrifuged at 750xg for 35 min with the acceleration at its lowest setting. The white interphase (buffy coat) between the plasma and Ficoll fractions was transferred into 35 mL 1X PBS and centrifuged for 10 min at 350 xg. The cells were then resuspended in 10 mL 1X PBS and centrifuged for 10 min at 250 xg. Cells were resuspended in 10% DMSO in heat-inactivated FBS (Life Technologies, cat # 10082139), frozen at −80C and then transferred to liquid nitrogen for long-term storage.

PBMC reprogramming to iPSCs

iPSCs were generated from donors via Yamanaka episomal-based reprogramming of peripheral blood mononuclear cells (PBMCs) (Lo Sardo et al., 2017). Isolated and cryopreserved PBMCs were thawed and cultured for 12-14 days in Mononuclear Cell (MNC) complete medium (MNC basal medium (IMDM (GIBCO Cat#21056023), Hams F12 (GIBCO Cat#31765035), Glutamax (GIBCO Cat#35050-061), Chemically Defined Lipid Concentrate (GIBCO Cat#11905031), ITS-X (GIBCO Cat#51500-056), 1-Thioglycerol (Sigma, 435uM), Bovine Serum Albumin (Sigma Cat#A9418, 0.5%w/v), and Ascorbic acid (Sigma Cat#A8960, 50ug/mL)) supplemented with rhEPO (R&D 2U/mL), hSCF (R&D 50ng/mL), rhIGF1 (R&D 40ng/mL), hIL3 (R&D 10ng/mL), Dexamethasone (Sigma Cat#D2915 1uM), and Holo-transferrin (R&D 50ug/mL)). Cell count was performed at feeding on Days 2, 5, 8, and 11, with cells seeded at 2.5×10^6 cells/mL for days 2-5, and 1.5×10^6 cells/mL on days 8 and 11. After 14 days of expansion 2×10^6 cells were transfected (Amaxa Nucleofector Technology) with plasmids containing the reprogramming transcription factors (pCXLE-hOCT3/4-shp53; pCXLE-hSK; pCXLE-hUL), 2ug each plasmid. Human CD34+ cells nucleofector kit (Cat#VPA-1003) was used with program U-008 on an Amaxa Nucleofector II device. Cells were allowed to rest in MNC complete medium for 2 days, then plated on inactivated MEF feeders (3×10^4 cells/cm^2) in MNC basal medium supplemented with 10% FBS, and transitioned to mTeSR1 medium (Stemcell Tech Cat#05850) over the next 3 days. Cultures were fed with fresh mTeSR1 on days 7, 9, and daily thereafter. From Days 10-20, 50% fresh mTeSR was supplemented with 50% fibroblast conditioned mTeSR (inactivated human foreskin fibroblasts (EMD Millipore Cat#SCC057)). Medium was supplemented with the small molecule enhancer of reprogramming sodium butyrate (0.25mM) as nascent colonies became visible with timing varying on a patient-by-patient basis, typically around Day 13. Colonies were allowed to develop until approximately 22 days post-transfection and then picked to feeder-free conditions on Matrigel (Corning Cat#354277), at which time sodium butyrate supplementation was stopped.

Induced pluripotent stem cells culture and characterization

Induced Pluripotent Stem Cells (iPSCs) were cultured in Matrigel-coated plates (Greiner Bio-one Cat#657160) with mTeSR medium. Cells were passaged every three to four days using 0.5mM EDTA as the dissociation reagent. PBMC-derived iPSCs were characterized after approximately 8-9 passages in culture. Karyotyping analysis was performed by Infinium HumanCore BeadChip. Validation of the iPS cells was performed by immunofluorescence staining and flow cytometry. 250,000 fixed cells per sample were incubated at room temp for 30 minutes in Blocking Buffer (5% heat inactivated FBS in 1XPBS, -Ca, -Mg). SSEA4 (Stemgent, Cat#09-0003, use 1:5) and TRA 1-60 (Millipore, Cat# MAB4360, use 1:100) were added to samples individually and incubated for 30 minutes RT. Three washes were performed with 1% heat inactivated FBS in 1XPBS, -Ca, -Mg. After the final wash, the SSEA4-stained samples were resuspended in 500 ul of Wash Buffer and transferred to FACS tubes. The TRA 1-60 samples were then resuspended in Goat anti-mouse-IgM Alexa 488 (Life Technologies, Cat#A21042, use 1:200) secondary, and incubated 30 minutes RT. Three washes were performed using the wash buffer listed above. The cells were resuspended in 500ul wash buffer and transferred to FACS tubes. The samples were read and analyzed on the LSR II. The LookOut® Mycoplasma PCR Detection Kit (Sigma, Cat. # MP0035) was used to check for Mycoplasma contamination, following the manufacturer's instructions and using JumpStart Taq DNA Polymerase (Sigma, Cat #D9307).

Genome editing, transfection, genotyping

Transcription activator-like effector nucleases (TALENs) for the 9p21 CAD risk region were designed using an archive of TALE modules as described (Miller et al., 2011), and cloned into a mammalian expression vector as fusions to obligate heterodimer forms of the FokI endonuclease (Doyon et al., 2011) bearing a TALE-FokI linker optimized for gene editing of endogenous loci in mammalian cells. The deleted region was designed to encompass all SNPs previously reported to be associated with coronary artery disease (rs1333039 (chr9:22065658) to rs1333049 (chr9:22125504). The flanking ∼5kb of these SNPs was tiled with TALENs to select the

best performing enzymes, resulting in the final coordinates of chr9:22062523-22129330. The TALENs were validated for genome editing activity at the endogenous locus in HEK293 cells by transient transfection of TALEN expression constructs followed by measurement of percentage of chromatids bearing a TALEN-induced insertion or deletion using a mismatch sensitive endonuclease assay, Surveyor/Cel1 (Guschin et al., 2010). 5′ capped and poly-adenylated mRNA coding for these TALENs was transcribed *in vitro* (Ambion Cat. AM1345), cleaned up using QIAGEN RNeasy (Cat. 74104), and delivered to iPS cell lines via electroporation using the Amaxa Nucleofector 2b device with Amaxa Human Stem Cell Kit 1 (Cat# VPH-5012) reagents. Cell lines were passaged using single-cell technique for two passages prior to transfection, using Accutase (Innovative Cell Tech, Inc, Cat. AT-104) to lift cells and 10μM Y-27632 dihydrochloride (ROCK inhibitor; Tocris Cat. 1254) in plating medium to protect cells. On the day of transfection, Accutase was used to produce a single-cell suspension, and 1.8-2x10^6 cells used in each reaction (passage 17). Reactions also contained 2.5μg mRNA for each TALEN in a given condition, and cells were transfected using the nucleofector program "A-024." Transfected cells were allowed to recover 24-48hrs before replating as single cells at low density (360 cells/cm^2) on Matrigel-coated plates. Individual subclones were then isolated and genotyped for editing status. Genotyping was performed by isolation of genomic DNA followed by PCR. Genomic DNA was extracted by lysis of cell pellets at 55C for ~1hr in tail lysis buffer (100mM Tris HCl (from pH 8.0 stock), 5mM EDTA, 200mM sodium chloride, 0.2% SDS, 290μg/mL proteinase K (Roche Cat. 03115828001)), treatment with RNase A (QIAGEN Cat. 1007885) at room temp. for 15min, separation of aqueous phase by phenol/choloform/isoamyl alcohol (Invitrogen Cat. 15593031) with 20min centrifugation at 4C and 15,000 RCF, precipitation with 3mM sodium acetate (Ambion Cat. AM9740) in 100% ethanol (Fisher Cat. BP2818), cleaning with 70% ethanol, and resuspension in TE buffer (Ambion Cat. AM9849) at 50C for ~1hr. Priming sites were located upstream and downstream of each TALEN cut-site, with internal priming sites deleted in successful CAD-risk allelic knock-outs. Primers sequences include: GJC 344F (5′ CATACAGGTCCCTGGCACTAA 3′), GJC 345R (5′ GAGCCAACGATATCTCCAAGA 3′), GJC 346F (5′ CGAAGGGCTTCCCTGTCTA 3′), and GJC 347R (5′ GACTTTCCCCCA CAATGAAA 3′). Genotyping PCR was performed using Herculase II polymerase (Agilent Cat. 600675) in 30uL reactions. Reaction parameters include: 40 cycles, 58C annealing, 20sec extension, 10ng genomic DNA template per reaction, and primer concentration of 250nM each. This assay allowed for detection of iPS clones with heterozygous or homozygous deletion of the 9p21 CAD-risk region by generating Sanger sequencing-verified products of unique size in the presence or absence of the CAD-risk region.

Smooth Muscle Cell Differentiation
iPSCs lines were differentiated as previously described in Cheung et al. (2014) protocol. Undifferentiated cells cultured in mTeSR medium were cultured in CDM-BSA 24h before seeding. Cells were seeded in CDM-PVA medium and differentiated through the lateral mesoderm lineage. After 17 days of differentiation cells were cultured in 10% FBS containing medium (DMEM (GIBCO Cat. 10566-016) supplemented with 10%FBS, Pen/strep (GIBCO Cat. 15140122), Glutamax (GIBCO Cat. 35050061), NEAA (GIBCO Cat. 11140050)) and passaged as a primary cell culture.

RNA extraction and qRT-PCR
Total RNA extraction from frozen or fresh cells was performed with the Trizol reagent (Invitrogen Cat.15596) and Zymo Direct-zol RNA miniprep kit according to manufacturer protocols. RNA was eluted in water and treated with Ambion DNA Free (Cat. AM1906) according to manufacturer protocols. cDNA for quantitative PCR was produced from isolated RNA using iScript cDNA Synthesis Kit (Bio-Rad Cat. 170-8891) in 20uL reaction volumes, according to manufacturer protocol. qPCR reactions were performed in 10uL final volume in 384-well plates, using iTaq Universal SyBr Green Supermix (Bio-Rad Cat. 1725121) for detection on a Bio-Rad CFX384 Touch Real-Time PCR machine. Each reaction was performed using cDNA template equivalent to 2-8 ng of total RNA, varying based on the expression level of each transcript of interest. Analysis was performed using a standard curve. A complete list of primers used for qPCR in Table S7.

Library Preparation for RNA sequencing
cDNA synthesis: Starting material used was 100ng of RNA. Followed Nugen's protocol using Nugen's Ovation RNA-Seq System V2 (Cat. 7102). Quality control was done using the DNA 1000 LabChip (Agilent Cat. 5065-1504).

Shearing: 1 ug of cDNA in 50 ul Buffer EB (QIAGEN, Cat. 1014612) was sheared using the Covaris S2 Focused Ultra-sonicator, Duty Cycle-10%, Intensity-5, Cycle/burst-200, time 100 s. The sheared cDNA was purified using 1.8X Agencourt ® Ampure® XP reagent (Beckman Coulter, Cat. A63882). Libraries were made using KAPA Hyper Prep kit for Illumina platform (Cat. KR0961) with Agilent's Sure Select XT2 adapters. The cycling parameters for amplification are: 98C-45 s 1 cycle, 98C-15S, 60C-30S, 72C-1min 4 cycles, 72C-1min 1 cycle, 4C hold. Library Quality control was done using the DNA 1000 LabChip (Agilent Cat #5065-1504). Libraries were normalized to 2nM and pooled. Final concentration of the denatured library pool was 10pM for the Rapid Run Mode and 12pM for the High Output mode. Sequencing was done on Illumina's HiSeq2500 (101X9X101 cycles). Approximately 40 million 2x100bp paired end reads were generated per condition and replicate.

ANRIL isoform amplification using template switching
We used a modified version of SMART-seq2 protocol to generate cDNA from SMCs.100ng of Total RNA was annealed with 0.5uM SMARTseq2-(dT)$_{30}$ primer and 1U of thermostable RNaseq inhibitor (Promega) in 10uL of RNase-free water (Ambion) for 2 minutes at 72C and placed on ice. Premade 10uL of 2x RT master mix with 1U Maxima H-reverse transcriptase (Thermofisher Scientific) and 1U

of RNasin Plus Thermostable RNase-Inhibitor (Promega), and template switch oligo (1uM final concentration) was added and mixed with annealed RNA on ice. The samples were placed into preheated to 42C thermocycler, and the following program run: 42C-30min; 2cycles of: 20C-5min, 42C-5min, 55C-10 min, 65C-5 min; 4C-hold. First round of PCR amplification was done by adding: 25uL Kappa HiFi ready mix (2x), 0.8uL 50uM ISPCR primer, 4.2uL H2O. Run program as follow (Dropseq protocol): 95C-3 min; 4cycles: 98C-20sec, 65C-45sec, 72C-3min; 9 cycles:98C-20sec, 67C-20seC, 72C-3min, 72C-5 min, 4C – hold. The library was cleaned with 1x AmpureXP beads and eluted in TE. Secondary PCR amplification was done with exons' specific primers with touchdown program: 98C – 1min; 8cycles: 98C-15sec, 68C-15sec (auto-delta −0.8 every cycle), 72C-3min; 34cycles: 98C-15sec, 60C-15sec, 72C-3min, 72C-3min, 4C hold. 10ng of RACE library was used as template. Primer pairs used: Exon1_fw – Exon13_rev. Complete list of primers in Table S6. The products were visualized on 1% agarose gel. The bands were cut and extracted using Zymo Gel DNA purification kit protocol with double wash with 750uL of DNA wash buffer.

ANRIL isoform overexpression

Reference isoforms 11 and 12 of *ANRIL* were ordered via gBlocks from IDT Inc. and minimal CMV promoter and KpnI and BsrGI digestion sites were added to the fragments by two rounds of PCR with Q5 polymerase, digested and inserted into 3rd generation lentiviral vector with tetracycline response element and truncated HIV 3'LTR. For lentivirus generation, LentiX HEK293T cells (Clontech inc.) at 70% confluency were transfected with 3rd generation packaging vectors (REV, RRE and pMD 2.G) and *ANRIL* plasmid using calcium phosphate method. 24 hours after transfection the media was changed to DMEM 10% FBS, supplemented with sodium pyruvate and nonessential amino acids and 1.1g/100ml of lipid free BSA (Sigma Aldrich). Virus was harvested 48h after transfection, filtered through 0.45um low protein binding syringe filters (Millipore) and concentrated using LentiX concentrator (Clontech) according to the manufacturer instructions. The pellets with the virus were resuspended in CDM-PVA media. NN KO cells at D13 of VSMC differentiation were co-infected with lentiviruses containing rtTA M2.2 and TetO_*ANRIL* 11 or 12. After 24 hours, 100ng/ml of doxycycline were added to the media to induce *ANRIL* expression. After D17 cells were maintained in VSMCs media with doxy for 4 more days. Cells were maintained in culture without doxy for 4 passages (about 20 more days). RNA was collected at passage 1, 2 and 4.

Deep sequencing and analysis of CAD Risk region

The region was divided into three parts 25, 25, and 16kb and each of them was amplified from genomic DNA using PrimeStar GXL enzyme using the following program: 98C – 1min; 8cycles: 98C- 15sec, 68C- 30sec (auto-delta −1every cycle), 68C-15min; 34cycles: 98C- 15sec, 60C- 30sec, 68C – 15min; 72C - 3min;4C – hold.

The fragments were separated on 1% low melt agarose (Biorad) and purified by Agarase (NEB) treatment and isopropanol precipitation. The PCR products were tagmented and amplified using NexteraXT (Illumina inc.) library preparation kit according to the manufacturers instructions. Fragments 550-600bp were selected using Bluepippin Prep (Sage Science) and sequenced with MiSeq using 2x300bp reads. The reads were aligned using Bowtie2 aligner and calls visually made using IGV.

RNA-seq data analysis

Adaptor sequences were removed using Trimmomatic PE v0.32. (Bolger et al., 2014). Reads were aligned using STAR aligner v2.3.0 (Dobin et al., 2013) to the human genome (hg19) and UCSC Genes reference transcriptome with default parameters. Read counts per gene were quantified with HTseq. (Anders et al., 2015). To remove genes with low expression levels, raw read counts were transformed to counts per million (CPM) and averaged within groups being compared. Genes with CPM values below 10 on average were excluded from the enrichment analyses and heatmaps. For differential expression analysis, raw counts were normalized using the variance stabilizing transformation and differentially expressed genes were identified using the DEseq function implemented in the DESeq2 R package (v1.8.2) (Love et al., 2014). For identification of *ANRIL* splicing junctions, we used samtools 1.3 (Li et al., 2009) to pool STAR aligned reads and IGV 2.3.80 (Integrative Genomics Viewer) (Thorvaldsdóttir et al., 2013) for visualization. A minimum of two reads must span a junction. For visualization batch effects were removed by the COMBAT function from the SVA R package (Surrogate Variable Analysis v3.18.0) (Leek et al., 2012)). The heatmaps were made using gplots. Principal component plots we generated with the rgl and pca3d R packages. Gene Ontology analysis was performed by using Panther Classification System (version 10.0 Released 2015-05-15) (Mi et al., 2013, 2016) (and DAVID Bioinformatics Resources 6.7) (Huang et al., 2009a, 2009b).

Methods for detection of circular RNA from RNA-seq datasets

The reads that were trimmed by Trimomatic as described before, were aligned using STAR aligner with parameters recommended by DCC package for paired and unpaired reads, as described on DCC's github page. The DCC package was executed without –R option to increase sensitivity. DCC @samplesheet –mt1 @mate1 –mt2 @mate2 –D –an genes.gtf –Pi –F –M –A genome.fa. The output tables with counts, coordinates and annotations were merge by locus d for further analysis.

Ingenuity Pathway Analysis

The Network and Canonical Pathway Analysis were generated through the use of IPA (QIAGEN Inc., https://www.qiagenbioinformatics.com/products/ingenuity-pathway-analysis/) (Krämer et al., 2014). The list of differentially expressed genes (3875) generated by DeSeq2 of RR VSMC versus [RR KO, NN, NN KO] was input on IPA software and analyzed. Canonical Pathways

with –log(p value) > 3 and with an absolute Z-score value of at least 2 were analyzed. For Canonical pathways and Network analysis shapes and lines were modified for simplicity.

Immunocytochemistry

Cultured cells were fixed using 4% paraformaldehyde in PBS. Fixed samples were treated with 0.5% Triton X-100 in PBS for cytoplasmic and nuclear staining. Cells were then blocked with 5% FBS in PBS for 1 hour at room temperature. Blocking solution was aspirated and replaced with primary antibody in blocking buffer and incubated approximately 2 hours at room temperature, or overnight at 4C. Primary antibody solution was then aspirated, fixed samples washed three times with PBS, secondary antibody and DAPI in blocking buffer added to the washed samples, and incubated 45min-1hr at room temperature. Three additional PBS washes were performed after secondary antibody incubation, and the samples imaged with fluorescence microscopy. In the case of phalloidin staining, the secondary antibody-treated samples were incubated for 30min with the phalloidin-Alexa conjugate (following manufacturer protocol), followed by two washes with PBS. Stained samples were imaged on a Nikon Eclipse Ti at 4x, 10x, and/or 20x magnification. Antibodies used include: Tra-1-81 (Millipore Cat. MAB4381, 1:500), TRA-1-60 (Millipore Cat. MAB4360, 1:500), Nanog (Abcam Cat. ab21624, 1:200), α-Smooth Muscle Actin (Sigma Cat. A5228, 1:1000), Phalloidin (Life Tech Cat. A12379, 1:50), Nkx2.5 (SCBT Cat. sc-14033, 1:200), Transgelin (TAGLN; Abcam Cat. ab14106, 1:500), Calponin1 (CNN1; Sigma Cat. C2687, 1:20,000).

DNA content Analysis

Cells at day 5 of VSMC differentiation were detached by using TrypLE Express (Life Technologies), spun at 200 g for 5 minutes. Pellet was washed in PBS and spun again. After PBS removal 70% cold EtOH was added dropwise while vortexing. Cells were incubated for 30 minutes at 4°C, and then spun at 200 g for 5 minutes at 4°C. After washing twice with PBS, pellets were resuspended in Propidium Iodide staining solution (0.1%Triton in PBS + 20ug/ml PI + 200ug/ml RNase A). Staining was performed overnight, and FACS analysis was performed the next day.

Cell Adhesion Strength Assay

25 mm glass coverslips (Fisher Scientific, St. Louis, MO) were cleaned via sonication with ethanol and DI water before being incubated with 0.1% gelatin in DI H$_2$O (StemCell Technologies, Vancouver, CAN) for 60 minutes at room temperature. After allowing cells to attach for 24 hours at 37°C and 5% CO$_2$, coverslips were then mounted on a custom-built spinning disc device (García et al., 1997) in a temperature-controlled spinning buffer (37°C) containing phosphate buffered saline with 0.5 mM MgCl$_2$ and 1 mM CaCl$_2$ (Cellgro, Manassas, VA) and 4.5 mg/mL dextrose (Fisher). Coverslips were spun for 5 min at defined angular velocities (2000, 3000, and 5000 rpm), fixed with 3.7% formaldehyde immediately after spinning, stained with 1:5000 Hoescht in DI H$_2$O for 15 minutes, and mounted with Fluoromount-G (Southern Biotech, Birmingham, AL). To obtain quantitative information of adhesion strength, coverslips were imaged at 10x magnification on a Nikon Ti-S microscope with motorized stage ($\sim$1000 individual images stitched together with Metamorph 7.6 software and custom macros) and cells positions from analyses performed by a custom written MATLAB script (Fuhrmann et al., 2014). The shear stress applied to each cell was computed based on their radial position using:

$$\tau = \frac{4}{5} r \sqrt{\rho \mu \omega^3} \qquad \text{Eqn (1)}$$

where r is the radial position from the center of the disk, ρ is the buffer density, μ is the buffer viscosity and ω is the rotational speed (Wen et al., 2014). Cell density as a function of radial position is normalized to a coverslip not subjected to shear and the center of each sheared coverslip. A sigmoidal fit is used to quantify adhesion strength, i.e., the point where 50% of cells remain attached.

Traction Force Microscopy

12 mm glass coverslips (Fisher) were oxidized via UV/ozone exposure (BioForce Nanosciences, Ames, IA) followed by functionalization with 20 mM 3-(trimethoxysilyl)propyl methacrylate (Sigma-Aldrich, St. Louis, MO) in ethanol. A polymer solution containing 10%/0.1% acrylamide/bis-acrylamide (Fisher), 1% v/v of 10% ammonium persulfate (Fisher), and 0.1% v/v of N,N,N',N'-Tetramethylethylenediamine (VWR International, Radnor, PA) was prepared. In addition, 2% v/v fluorescent 580/605 0.2 μm microspheres (Invitrogen, Carlsbad, CA) were added to the pre-polymer solution. 7 μL of polymerizing hydrogel solution was sandwiched between a functionalized coverslip and a dichlorodimethylsilane-treated glass slide and was allowed to polymerize for 15 minutes. 0.1% gelatin (StemCell Technologies) was coupled to the surface using N-sulphosuccinimidyl-6-(4'-azido-2'-nitrophenylamino) hexanoate (sulfo-SANPAH) as a protein-substrate linker. Hydrogels were incubated in 0.2 mg/ml sulfo-SANPAH (Fisher) in sterile 50 mM HEPES pH 8.5, activated with UV light (wavelength 350 nm, intensity 4 mW/cm^2) for 10 minutes, washed three times in HEPES, and then incubated in 0.1% gelatin (BD Biosciences) overnight at 37°C. Following UV sterilization, cells were cultured on substrates for 48 hours at 37°C and 5% CO$_2$. The microspheres underneath selected live cells were imaged with a 60x water confocal objective using a Nikon Eclipse TI-S microscope equipped with a CARV II confocal system (BD Biosciences) and motorized stage. Images were acquired on a Cool-Snap HQ camera (Photometrics) controlled by Metamorph (Molecular Devices). Cells were released with

2.5% trypsin (Fisher) and the same confocal stacks acquired. Bead displacements were determined using a particle image velocimetry script in MATLAB (MathWorks) and normalized to cell area.

Gel Contraction Assay

Cells were detached from substrates using Tryple (Thermo Fisher Scientific, Waltham, MA) as previously described and suspended in 1x DMEM (Thermo) containing 10% fetal bovine serum (Gemini Bio-products, West Sacramento, CA). 80 μL of 6x DMEM, 400 μL of 3 mg/mL type 1 rat tail collagen (Corning Incorporated, Corning, NY), and 120 μL of cell suspension at a final concentration of 0.2 million cells/mL were placed in a 24-well plate and allowed to polymerize at 37°C and 5% CO_2 for one hour. To assess smooth muscle cell contractility in the presence of contractile agonist and antagonist, a final concentration of 10 nM bradykinin or 0.5 μM cytochalasinD (Sigma-Aldrich, St. Louis, MO) was added to cell suspension media. After 24 hours at 37°C and 5% CO_2, 1mL of 1x DMEM + 10% FBS was added to each well. Images of the gels were taken at each subsequent 24 hour period until 8 days in culture. The diameter of each gel was measured using ImageJ software (NIH, Bethesda, Maryland) and normalized to the initial gel diameter on day 0.

QUANTIFICATION AND STATISTICAL ANALYSIS

Statistical analysis

Statistical analyses were performed using GraphPad Prism5 and detailed in the corresponding figure legends and number experiments and samples for each experiments is detailed in Table S2. Data were analyzed by one-way ANOVA followed by Bonferroni's multiple comparison post hoc test or t test as specified in the corresponding figure legends. Data for significance of CAD-associated genes from GWAS studies in Figure 7 were analyzed with binomial distribution test in R.

DATA AND SOFTWARE AVAILABILITY

The accession number for the RNA-seq data reported in this paper is GEO: GSE120099

Supplemental Figures

Figure S1. 9p21.3 CAD Deletion iPSCs Generation and Validation, Related to Figure 1

(A) Schematic of the genotyping PCR performed to detect 9p21 deletion and genotyping results. Two possible products (400bp WT, and 300bp KO) can be amplified in the presence or absence of the intact 9p21 region. The panel shows the genotype of 2 WT, 2 heterozygous deleted and 2 KO iPSC clones derived from both donors.

(B) Table summarizing the number of iPSC lines screened for editing and the efficiency of 9p21 deletion for each donor (RR and NN) and for each TALEN set.

(C) Sequencing diagram shows the TALEN cut site location on different iPSC clones.

(D) Graphs show normalized counts for *CDKN2A, CDKN2B, ANRIL (CDKN2B-AS1)* from RNA-Seq of iPSC lines.

(legend continued on next page)

(E) In scale figure showing complete CAD risk region difference between the two patients validated by deep Next Generation Sequencing. The index SNPs of the risk status are highlighted with yellow, and non-risk specific SNPs are highlighted in green. Only homozygous SNPs are shown. 83 total differences were observed between individuals, 57 are directly associated with 9p21 risk status (R-squared > = 0.8 with index allele rs23832207). For the remaining 26 SNPs, 25 are common variants (R-squared < 0.8, allele frequency > 5%), and one is a rare variant (rs72652428) with frequency < 1%.

(legend on next page)
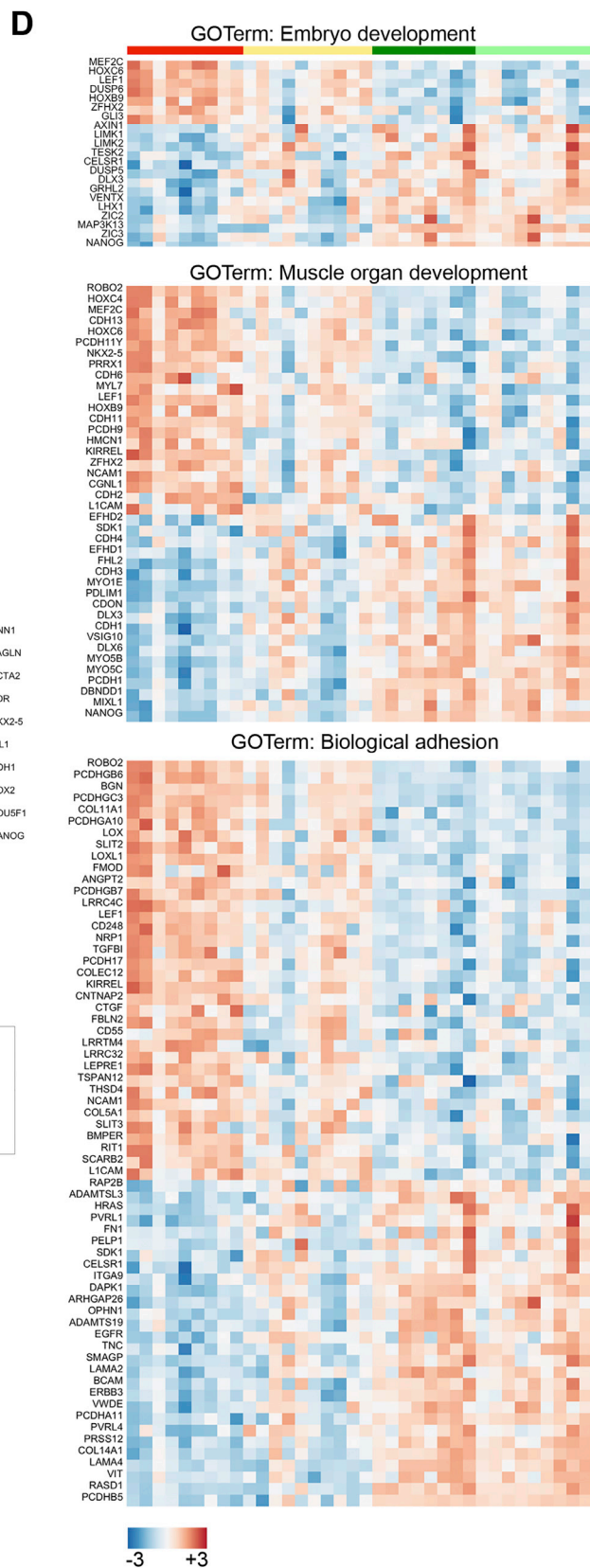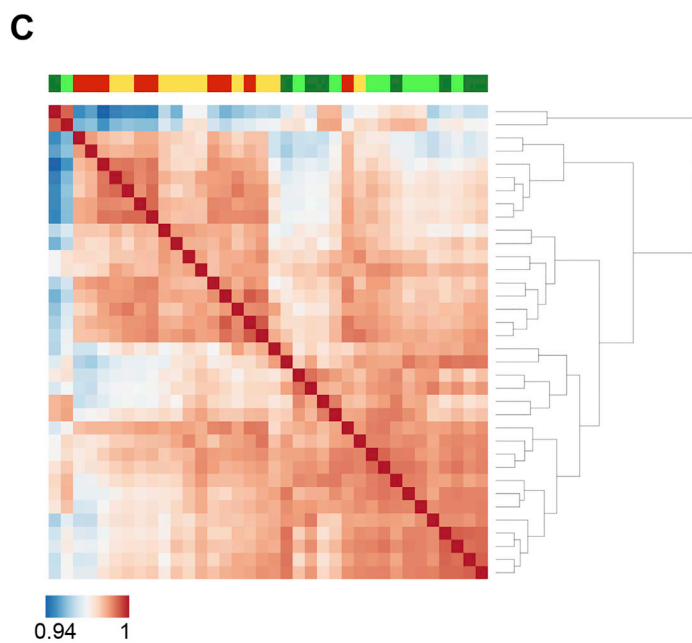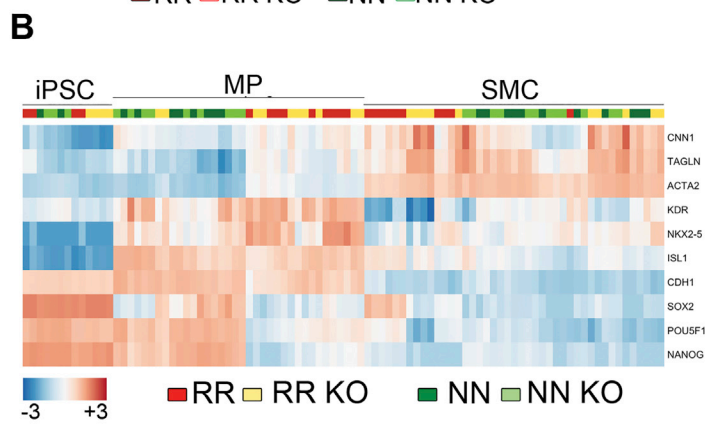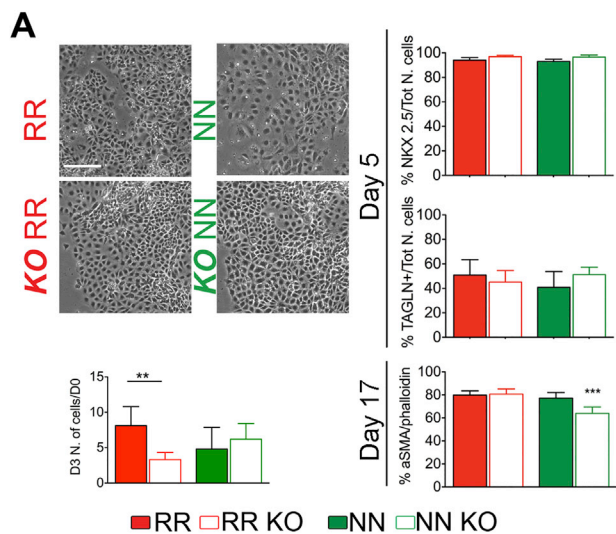
Figure S2. Smooth Muscle Cell Differentiation of 9p21 KO iPSCs and Phenotype at Mesodermal Progenitor Stage, Related to Figure 2

(A) Phase contrast images of mesodermal progenitor cells at D5 of differentiation. Bar is 200 μm. Cell count at day 3 of the VSMC protocol for the 4 different genotypes (bottom left graph). Quantification of NKX 2.5 and TAGLN positive cells at day 5 of the differentiation protocol performed by imaging and counting (right top and middle graphs). Quantification of alpha-SMA positive cells at D17 performed by imaging and counting. Phalloidin was used for normalization. Quantification was performed by measuring the area covered by alpha-SMA signal normalized to phalloidin staining (right bottom graph). The bars show mean ± 95% CI of one or two independent experiments. For each experiment 2-3 lines were used per genotype. *p < 0.05; **p < 0.001: ***p < 0.0001 one way ANOVA-Bonferroni. Details about number of lines can be found in Table S2.

(B) Heatmap of key genes in three stages of VSMC differentiation: iPSCs, MP and terminally differentiated VSMCs.

(C) Heatmap showing hierarchical clustering of transcriptome similarity of MP at day 3.

(D) Heatmaps of genes differentially expressed in MP at D3 from the GO category Embryo development (p = 2.58E-02, fold enrichment 2.57), Muscle organ development (p = 3.44E-05, fold enrichment 2.55), Biological adhesion (p = 1.63E-04, fold enrichment 1.94).
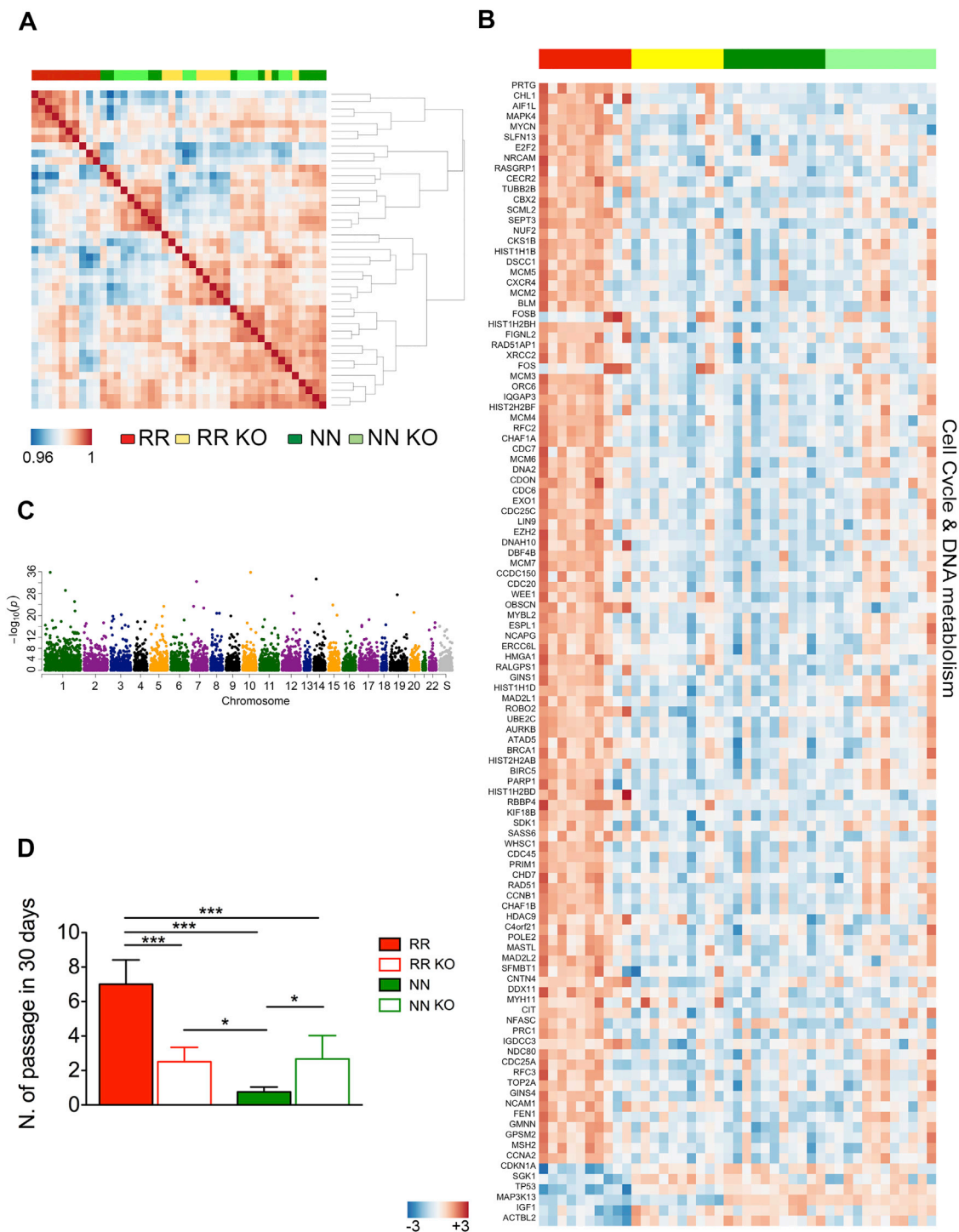
Figure S3. Terminally Differentiated VSMC, Related to Figure 3

(A) Heatmap showing hierarchical clustering of transcriptome similarity of VSMC at D17.

(B) Heatmaps showing genes differentially expressed in the presence of RR 9p21 at D17 (fold change > 2), included in the following GO categories: Regulation of cell cycle (GO:0051726), (fold enrichment = 9.03, p = 9.19E-04); DNA recombination (GO:0006310) (fe = 5.87, p = 2.57E-03); DNA replication (GO:0006260) (fe = 4.92, p = 6.86E-09); DNA metabolic process (GO:0006259) (fe = 3.33, p = 3.94E-09); DNA repair (GO:0006281) (fe = 3.07, p = 8.45E-03); chromatin organization (GO:0006325) (fe = 2.47, p = 4.28E-02); cell cycle (GO:0007049) (fe = 2.23, p = 2.60E-09). Values are Z-score.

(C) Linear Manhattan Plot showing the distribution of differentially expressed genes in the presence of Risk 9p21.3 throughout the genome at D17.

(D) VSMC proliferation analysis as number of passages of mature VSMCs in culture in 30 days (mean ± SD). *p < 0.05; ***p < 0.0001 one way ANOVA-Bonferroni.
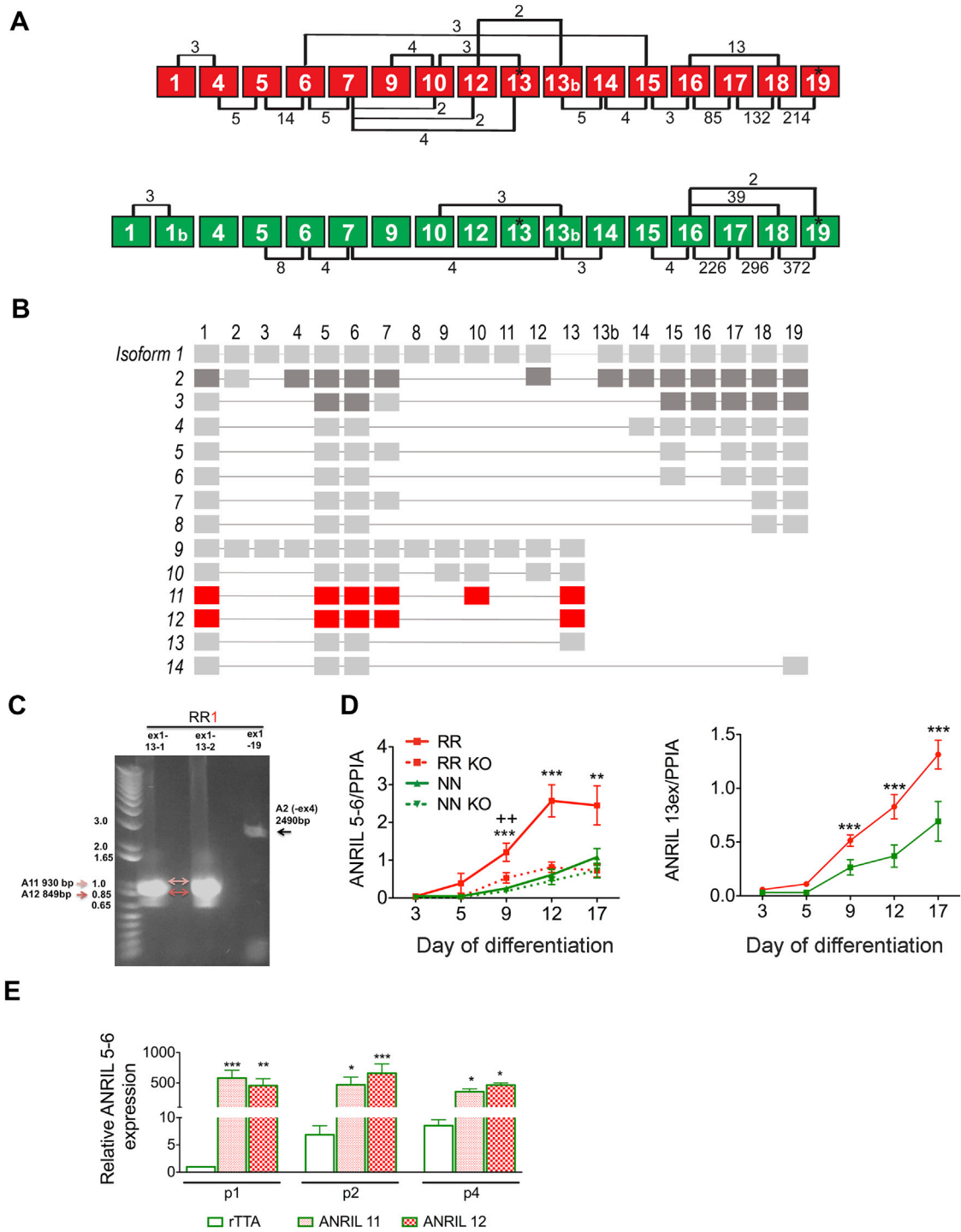
Figure S4. Analysis of *ANRIL* Isoforms and Overexpression Experiment, Related to Figure 5

(A) Schematic of *ANRIL* exon-exon junction reconstruction in RR (red) and NN (green) VSMCs. Lines represent junctions between exons identified by mapping RNaseq reads. Numbers are the number of reads for each junction. * indicates termination site, at exon 13 and exon 19.

(B) Schematic of *ANRIL* splicing isoforms. Light gray represents *ANRIL* isoforms previously described. Dark gray highlights isoforms present in VSMCs in our study, based on aligning RNA sequencing reads across exon junctions. *ANRIL* 11-12 isoforms highlighted in red were confirmed also by RT-PCR. RNaseq results (summarized in Figure 5A) show novel alternative splicing in isoforms 2 and 3. In particular, *ANRIL* 2 isoform does not contain exon 2 and 4, and there is evidence for possible usage of exon 12 in RR.

(legend continued on next page)

(C) Agarose gel showing RT-PCR results for *ANRIL* isoforms. PCR was performed using primers spanning exon 1 through exon 13, or exon 1 through 19. cDNA template was from the RR1 donor. On the left side DNA ladder, arrows show isoforms identified after Sanger sequencing of the gel extracted bands.

(D) Quantification of *ANRIL* expression using primers in the 5-6 exon junction (left) and within exon 13(right) (relative to samples presented in Figure 5B). (E) qRT-PCR detecting *ANRIL* expression (exon 5-6 junction) in NN KO cells after rtTA, rtTa+ ANRIL 11 or 12 transduction at passage 1, 2, 4. Graph shows expression of *ANRIL* relative to rtTA control at p1. PPIA was used as reference gene. Data are mean of two independent replicates. Bar is SEM. *$p < 0.05$, **$p < 0.01$ ***$p < 0.001$.
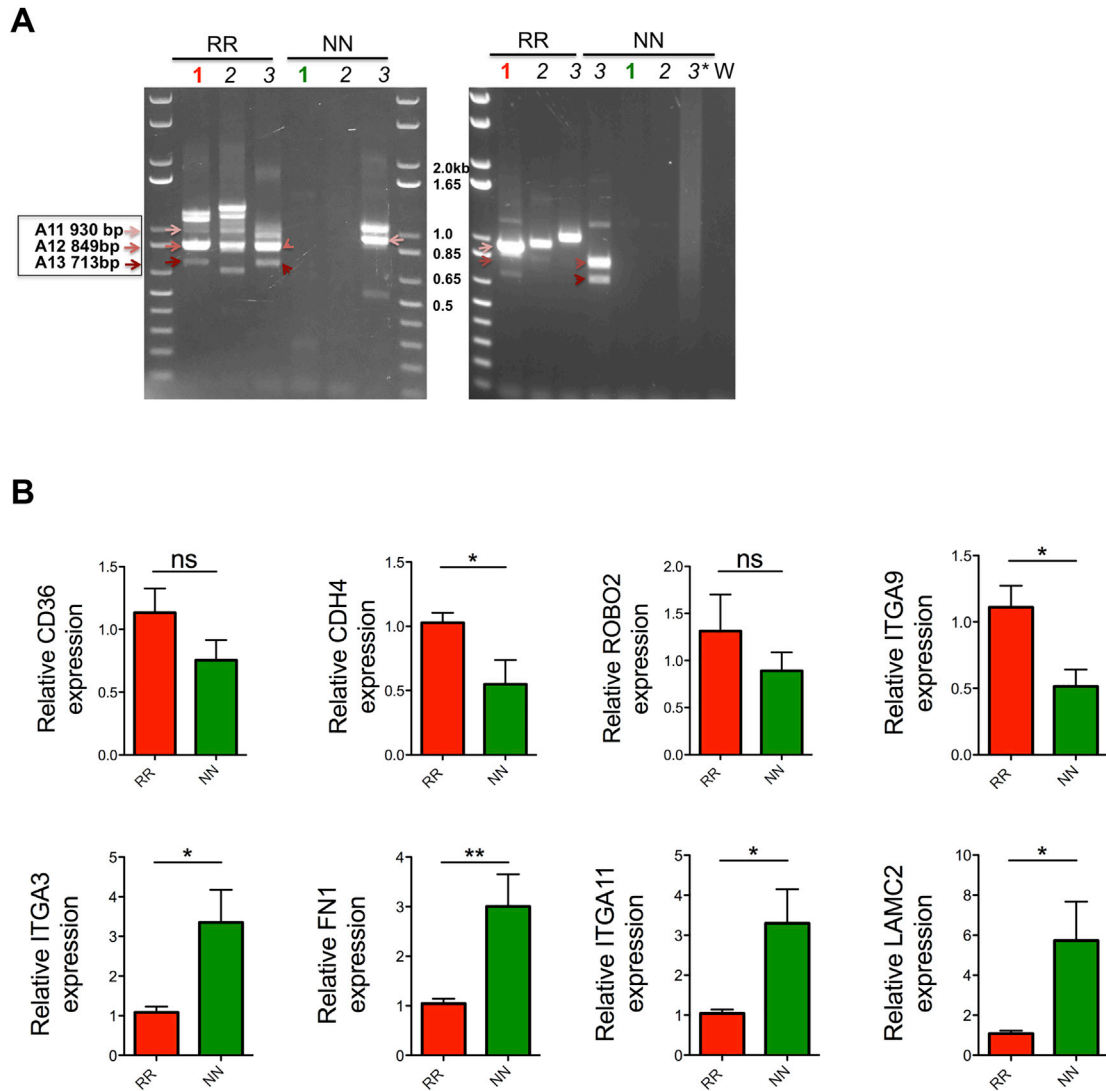
Figure S5. Validation of Gene Expression Analysis on Additional iPSC-Derived VSMCs from Independent Donors, Related to Figure 6

(A) RT-PCR for *ANRIL* performed with primers spanning exons1 through 13. Samples used are 3 RR and 3 NN VSMC (D17) from donors described in Figures 1 and 6 and Table S2. Gels show two RT-PCR of 42 cycle after a 26 cycle RACE from 2 independent library preparations. Arrows of different colors represent different *ANRIL* isoforms (A11, A12, A13). "NN 3*" in the gel on the right is an additional reaction of NN 3 sample in which more DNA was used. Details about exon composition of the isoforms can be found in Figure S4B.
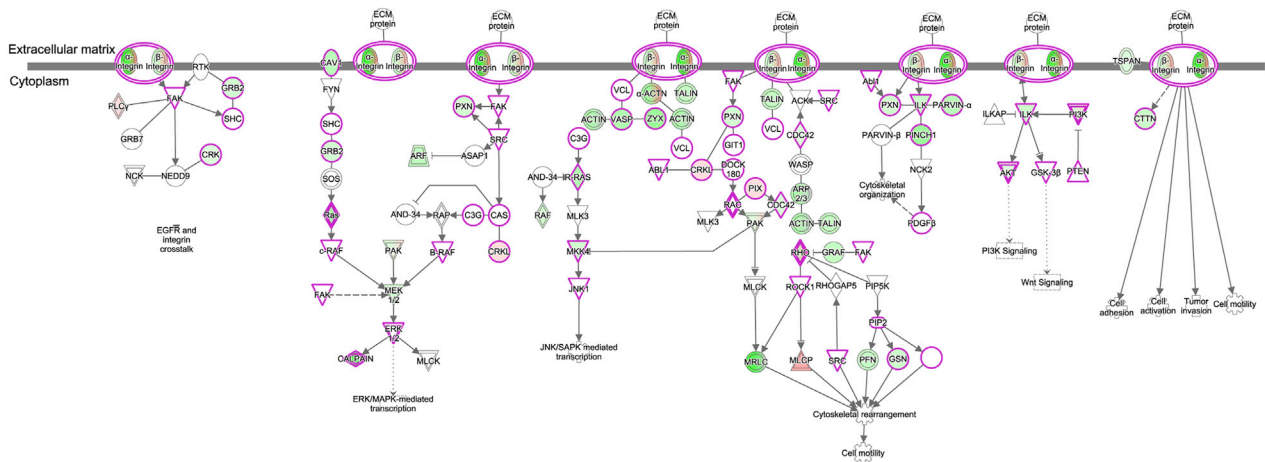
(B) qRT-PCR analysis of adhesion molecule genes was performed on additional RR and NN lines described in Figure 6 (mean ± SEM). *p < 0.05 and **p < 0.01 unpaired t test.
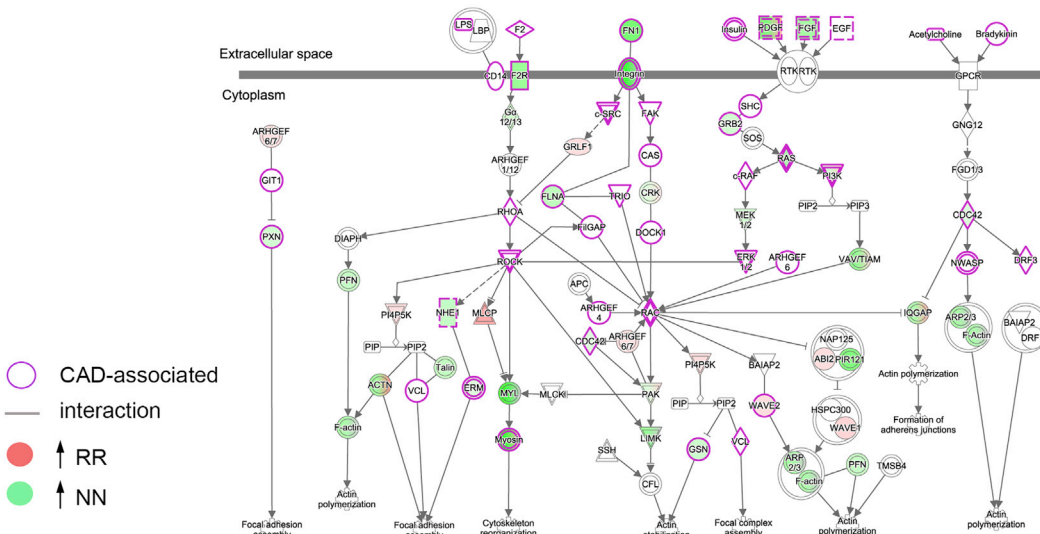
A
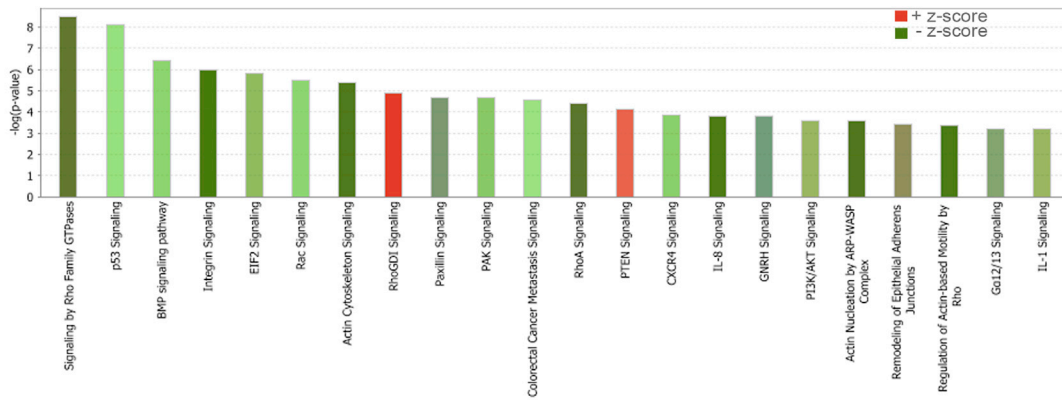
B

Integrin Signaling

C

Actin Cytoskeleton Signaling

(legend on next page)

Figure S6. Relevance for Cardiovascular Disease, Related to Figure 7

(A) Graph shows Canonical Pathways from IPA Analysis. Pathways with –log(p value) > 3 and a Z-score absolute value of at least 2 are shown. Red and green indicate positive Z-score (pathways upregulated) and negative z-score (pathways downregulated) in RR VSMCs compared to the other three genotypes (RR KO, NN, NN KO). Using the same analysis parameter the control gene list resulted in only one pathway (PI3K/AKT Signaling).

(B) Integrin Signaling.

(C) Actin Cytoskeleton Signaling from IPA canonical pathway analysis.
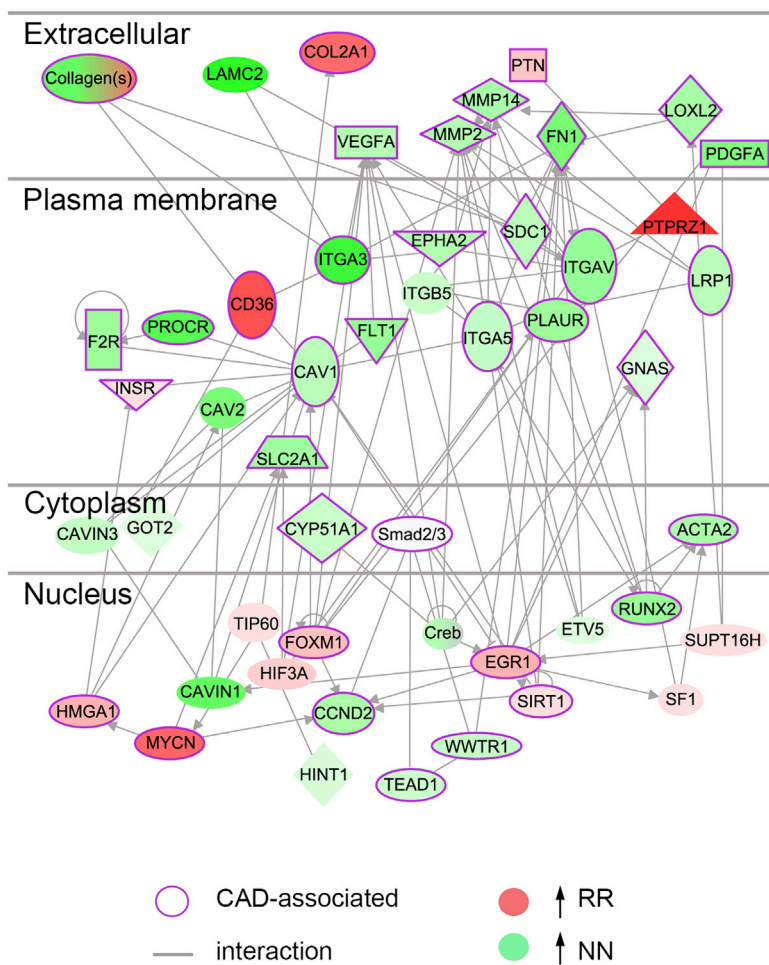
Figure S7. *De Novo* Gene Interaction Network, Related to Figure 7

(A) De novo interaction network by IPA. This network was enriched for terms including "Cellular Movement, Cardiovascular System Development and Function, Cardiovascular Disease."